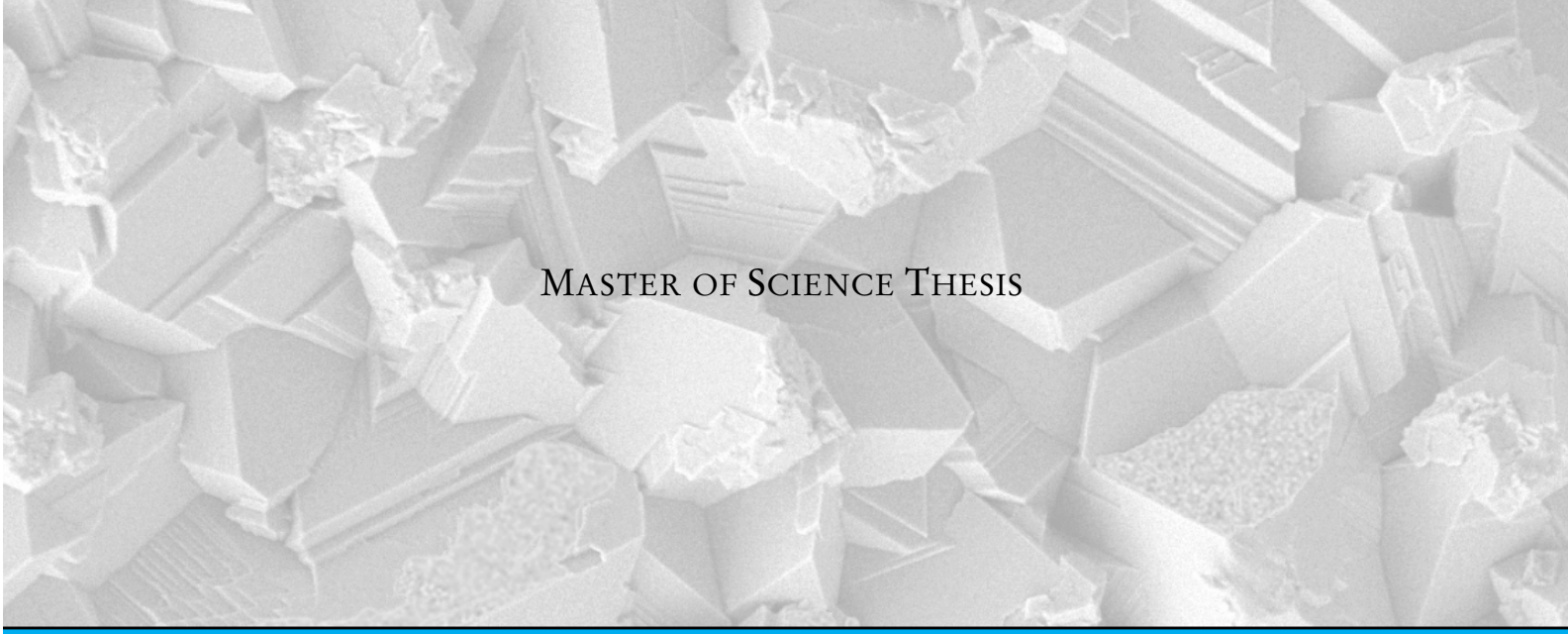

MASTER OF SCIENCE THESIS

Structure property relationships for NTC ceramics (I) and polymer composites (II)

D.B.Deutz

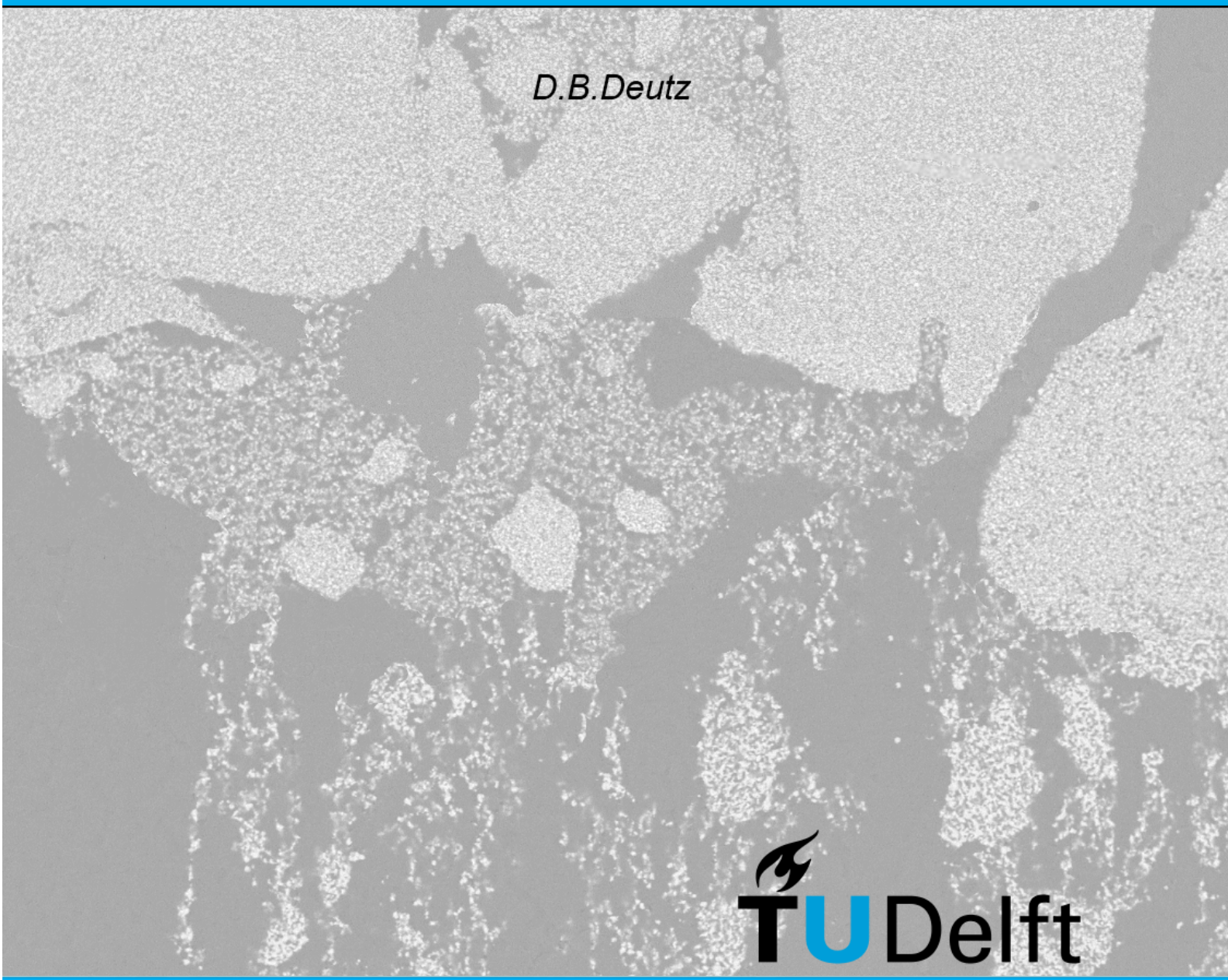

TU Delft

Faculty of Aerospace Engineering

Delft University of Technology

Structure property relationships for NTC ceramics (I) and polymer composites (II)

Master of Science Thesis

For obtaining the degree of Master of Science in Aerospace Engineering at the Delft University of Technology

author:	D.B. Deutz
supervisors:	Ir. H. Khanbareh
	Prof. dr. W.A. Groen
	Prof. dr. ir. S. van der Zwaag

Date:	March 8, 2013
Student number:	1221086

Contact information: Daniella.Deutz@gmail.com

ABSTRACT

Negative temperature coefficient of resistance (NTC) materials experience a change in resistance upon a small change of temperature. These materials find wide application in temperature sensors and are generally based on nickel manganite ceramics.

In this study, both NTC ceramics and NTC polymer composites are examined. The long term room temperature stability and aging at 125°C of NTC ceramics is investigated. A microstructural analysis of the phase formation of NTC ceramics is presented.

Electrically conductive NTC polymer composites are developed based on nickel manganite calcined powder and Epotek epoxy. Processing NTC polymer composites with dielectrophoresis is investigated. The nature of the connectivity occurring within the NTC polymer composites is examined through interparticle distance calculations and comparisons with existing models.

CONTENTS

NOMENCLATURE

Acronyms

BEC	backscattered electron composition
CFSE	crystal field stabilization energy
CTE	coefficient of thermal expansion
DEP	dielectrophoresis
DGEBA	diglycidyl bisphenol-A
FE-SEM	field emission - scanning electron microscope
FGC	functional granular composites
GEM	general effective media
IC	integrated circuit
NTC	negative temperature coefficient of resistance
OEW	operational empty weight
PANI	polyaniline
POPD	poly(oxypropyl)-diamine
PTC	positive temperature coefficient of resistance
PZT	lead zirconium titanate
RTD	resistance temperature detectors
SEM	scanning electron microscope
SMD	surface mounted device
TGA	thermal gravimetric analysis
XRD	x-ray diffraction

Glossary

Latin Symbols

Name	Unit	Description
A	Ω	Resistance of a NTC at infinite temperature
A	m	Electrode area
A	-	Bruggeman-GEM model constant
a	nm	Electrical transport distance
a	m^2	Contact spot area
B	K	Material constant of a NTC
c	-	Probability
d	m	(Particle) diameter
E	GPa	Elastic modulus
E_a	eV	Activation energy for electrical conductivity
E_μ	eV	Activation energy of polaron conductivity
F	N	Force
G	m	Geometry factor
H	-	Contact hardness
k	eV/K	Boltzmann constant
L	m	Length
M	-	Number of particles forming one conduction path
N	-	Number of conduction paths
Q	V/K	Thermopower
R	Ω	Resistance as a function of temperature
T	K	Temperature
t	m	Thickness
w	m	Width

Greek Symbols

Name	Unit	Description
α	%/K	Sensitivity coefficient, or temperature coefficient of resistance
β	-	Degeneracy factor involving spin and the orbital degeneracy of the electronic carrier
γ	-	Degree of inversion
Γ	-	Particle size to sample thickness ratio
ν	Hz	Phonon frequency
ρ	Ω.m	Resistivity
ρ_∞	Ω.m	Resistivity at infinite temperature, aka specific resistivity
σ	S/m	Electrical conductivity
ϕ	%	Volume content of filler
ϕ_c	%	Critical volume content of filler
ξ	-	Empirical value for contact diameter deformation

Subscripts

Name	Description
c	Composite
cr	Constriction
e	Lead
h	Insulating polymer matrix
i	Intrinsic
l	Conductive filler
m	Composite
p	Particle-particle

LIST OF FIGURES

LIST OF TABLES

CHAPTER 1

GENERAL INTRODUCTION

Monitoring and adjusting the temperature is part of daily life and routine in both domestic and industrial settings. Commercially available temperature sensors used in aerospace, automotive and general applications can be divided into three groups: thermoelectric devices (thermocouples), electrical resistance devices (resistance temperature detectors (RTD)'s and thermistors), and semiconductor devices (integrated circuit (IC) sensors). Thermocouples are the most common type of temperature sensor since they are small, robust, relatively cheap, and can cover the widest temperature range. However, they are active sensors, susceptible to corrosion degradation, require precision amplification, and a reference temperature. RTD's are highly accurate passive sensors, yet due to the use of platinum, are also the most expensive temperature sensor available. Beside their cost, the major disadvantages of RTD's are their extremely slow response time as well as a relatively low sensitivity to small temperature changes. IC sensors are also passive sensors like RTD's, and while their response time is fast, their accuracy leaves much to be desired. [1–3]

Thermistors offer the highest temperature sensitivity when a passive, quick and low cost sensor is required. To meet the requirements of each environment and application, thermistors can be geometrically, but also chemically tailored (see Figure 1.1, which shows a small selection of commercially available thermistors).

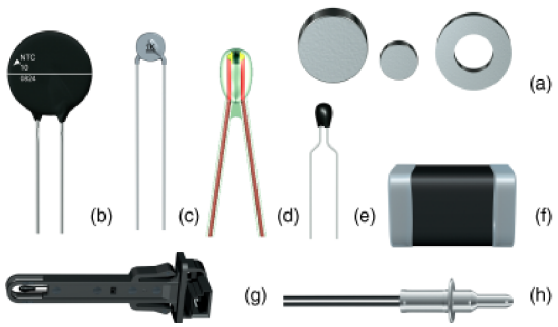

Figure 1.1: Examples of NTC components: (a) leadless, (b,c) lead space, (d) glass encapsulated, (e) resin-encapsulated, (f) surface mounted device (SMD), and (g,h) probe sensors. [1] (Courtesy of EPCOS AG, Germany)

Thermistors made from semiconducting mixed-valence metal-oxides utilize a characteristic negative temperature coefficient for temperature sensing, and are commonly referred to as negative temperature coefficient of resistance (NTC) ceramics or simply: NTC's. Before NTC's could be mass produced, the influence of impurities, dopants and heat treatments on the electrical characteristics along with the time dependent resistivity, or aging, had to be investigated. One of the first stable NTC's to be mass produced were nickel manganite NTC's.

Since their discovery, a considerable amount of research has been performed to better understand nickel manganite NTC's. The most comprehensive phase diagram for the nickel manganite system dates back to 1964, and provides a reasonable baseline for predicting the electrical behavior of nickel manganite ceramics (Figure 1.2). While there have been many studies into the exact cation distribution and the semiconductivity of nickel manganite NTC's both remain major sources of discussion. Additionally, the time dependence of the resistivity has not been investigated over prolonged periods of time. [4]

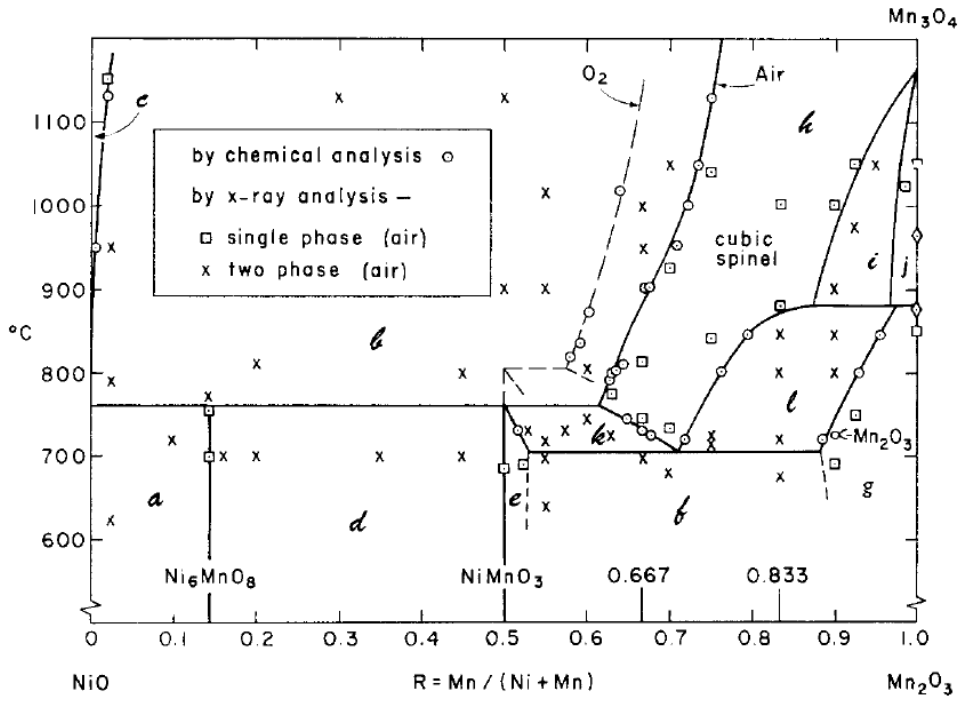

Figure 1.2: Phase diagram of Ni-Mn-O developed by Wickham in 1964 [5].

Apart from the many advantages afforded by NTC thermistors, there is one major drawback: they are made from heavy ceramics. In aerospace, weight is an incredibly important factor in designing an aircraft. Every kilogram of the operational empty weight (OEW) that can be spared is matched by an equal increase of the maximum payload the aircraft can carry. [6] This explains why metal and ceramic components are being replaced by light weight composites as they become available (Figure 1.3).

Besides their high weight, thermistors are inherently stiff, brittle, and require high temperatures and complex processing to manufacture. Composites, on the other hand, are relatively simple to produce into any number of shapes, while retaining mechanical flexibility. One step composite production can be employed to integrate both functional and structural properties into a single part, further decreasing the overall weight of the aircraft. The secondary properties of composites, such

as improved fatigue behavior and corrosion resistance, are also a driving force for their implementation. [6]

A material that could combine the high sensitivity of traditional NTC thermistors with the flexibility of design and weight savings offered by composites would be welcomed by the aerospace industry.

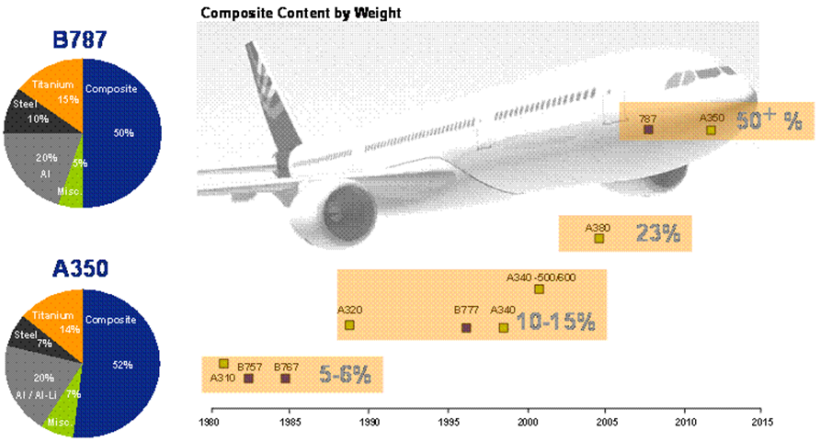

Figure 1.3: Importance of composites for the aerospace industry (Courtesy of Hexcel).

This thesis will investigate both the effects of long term room temperature aging on nickel manganite NTC ceramics in Part I, and the prospects of producing flexible and lightweight alternatives in Part II, that retain the fast response time and sensitivity characteristic to NTC thermistors.

Part I

Phase Formation and Aging of Nickel Manganite NTC Ceramics

CHAPTER 2
INTRODUCTION

2.1 NTC ceramics

The electrical conductivity of negative temperature coefficient of resistance (NTC) increases as the temperature rises. The dependence of the resistance on temperature in NTC's is highly nonlinear, as Figure 2.1 shows, in comparison to positive temperature coefficient of resistance (PTC) and resistance temperature detectors (RTD). [7] The resistance of an NTC is not only determined by its geometry, but also by the characteristic resistivity of its composition.

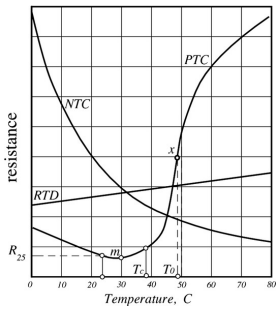

Figure 2.1: Comparison of the resistance of PTC, NTC and RTD as a function of temperature. [7]

In general, nickel manganite NTC's have a low characteristic resistivity and are relatively easy to manufacture, which makes them an attractive composition in industry for the production of temperature sensors. This part of the thesis will focus on investigating the differences between long-term room temperature stability and short term aging of sintered nickel manganite NTC ceramics. Sintering schemes and their effect on the conductivity of NTC ceramics are studied. A composite SEM micrograph of multiple sintered ceramics is shown and the phase distribution is presented and compared with expectations from XRD diffractograms and the reported phase diagram. Finally, the effects of long-term room temperature aging on NTC bulk ceramic conductivity are investigated.

In the next section, a literature review will be presented on general NTC bulk ceramic behavior and stability. This is followed by an investigation into the electrical properties and phase distribution of NTC bulk ceramics as a function of their sintering scheme in chapter 3. A discussion of the results garnered from NTC bulk ceramic testing will then be presented in chapter 4.

2.2 Literature review

In this thesis, NTC bulk ceramics of the nickel manganite family have been used to study the effect the preparation scheme has on phase formation and electrical stability. This NTC family has its own peculiar properties, and must first be understood before any investigation can take place. To that end, a short review is presented on the crystal structure in subsection 2.2.1, the electrical properties in subsection 2.2.2, and the specific conduction mechanism in subsection 2.2.3. Finally, the stability issues inherent to NTC's are given in subsection 2.2.4.

2.2.1 Crystal structure and cation distribution

There are only a minute amount of crystal structures capable of producing the temperature dependent resistance response that define NTC ceramics as a separate class of electroceramics. In this study, ceramic powder of the $Mn_{3-x}Ni_xO_4$ family has been used, which crystallizes in the spinel structure.

The spinel crystal structure, denoted by AB_2O_4, owes its name to the spinel mineral: $MgAl_2O_4$. It was determined independently by Bragg [8] and Nishikawa [9] to belong to the cubic space group *Fd3m* ($F^4_{1/d}\,\bar{3}_{2/m}$; O^7_h; Number 227 in the International Table of X-ray Crystallography). The spinel structure is a cubic close packed (FCC) lattice with $8[AB_2O_4]$ units in its unit cell. It is normally comprised of 32 large O anions coordinated by 24 metal cations which occupy 8 tetrahedral interstitials (A-sites) and 16 octahedral interstitials (B-sites). This means that only 1/8 of the tetrahedra and 1/2 of the octahedra are occupied. The positions of the filled interstitials are generally fixed, and arranged so that tetrahedra share corners with octahedra, and octahedra share edges with each other. This has consequences for the bond lengths between the cations, which are given by B-B: $\frac{\sqrt{2}}{4}\alpha_0$, A-A: $\frac{\sqrt{3}}{4}\alpha_0$, and A-B: $\frac{\sqrt{11}}{8}\alpha_0$ where α_0 is the lattice parameter. [1] For cubic spinels, the lattice parameter is normally between 8.05Å and 8.50Å. [10]

The cations in the B-sites have a great effect on the electrical conductivity, since the (B-B) distance between them is the shortest. Most of the time the B-sites are filled by trivalent cations, while the A-sites contain divalent ions, although any combination of divalent, trivalent or quadrivalent ions is possible. The cations can also be the same metal under different valence charges. The positions of the occupied interstitials are mostly fixed, but the exact distribution of the A and B cations can differ.

The density of spinels depends on the atomic mass, but also on the cell volume, which in turn depends on the ionic radius and cation distribution of its constituents. In general, nickel spinels tend to have smaller lattice parameters because nickel is the smallest divalent ion. Spinels containing manganese cations have the largest cell volume because of its large ionic radius. Densities for spinels normally range from 4.4 to 5.4 g/cm^3. [11]

Spinels are happy to accommodate a great deal of cation disorder. Two limiting configurations of cation distributions have been defined, named 'normal spinel' and 'inverted spinel', which constitute the outer limits of the possible cation disorder. [12] The configuration of each is:

Normal spinel: $[A]^{tet}[B_2]^{oct}O_4$ (illustrated in Figure 2.2),
Inverted spinel: $[B]^{tet}[AB]^{oct}O_4$.

In order to be able to differentiate between different cation distributions the parameter γ, or the degree of inversion, was introduced, which defines the fraction of A ions on the octahedral sites. The

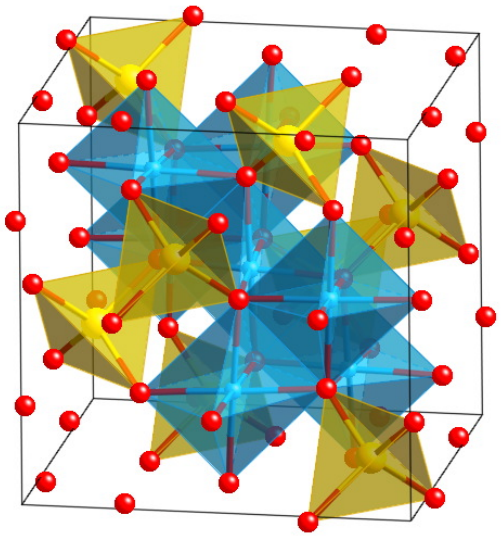

Figure 2.2: Spinel cubic unit cell of $MgAl_2O_4$ showing O in red, Al in blue, and Mg in yellow; tetrahedral and octahedral coordination polyhedra are highlighted. (Created in CrystalMaker software)

degree of inversion for normal spinels is equal to 0, while for inverted spinels it is equal to 1. Further, the flexibility of the spinel crystal structure allows γ to take all possible non-integer values between 0 and 1. These cation distributions are often termed 'random spinel', and an example of such a random distribution is: $[B_{0.44}A_{0.56}]^{tet}[A_{0.44}B_{1.56}]^{oct}O_4$, where $\gamma = 0.44$.

Several factors influence γ, including the site preferences of ions in terms of size, covalent bonding effects, temperature effects, and most importantly, the crystal field stabilization energy (CFSE).

Crystal field stabilization energy

The crystal field stabilization energy is the stability that results from placing a transition metal ion in the electrostatic field (or crystal field) generated by a set of ligands (negatively charged ions surrounding and interacting with the free ion). The stabilization occurs as a result of the electrostatic repulsion between the free ion and the ligands.

In a number of electron configurations, the stabilization of the crystal field can be increased by physically displacing the ligands around the transition-metal ion. The displacement is minimal, but destroys the symmetry of the configuration of ligands. This tetragonal distortion of the octahedral geometry is called the Jahn-Teller effect, and is the strongest for d^9, d^7 (low spin only) and d^4 (high spin only) ions. [13–15]

If one of the constituents of a spinel compound is a transition-metal ion, and this ion has a relatively large CFSE (that energy being some fraction of Δ_{oct}), then this ion will compete to occupy octahedral (or B) sites. The crystal will deform even if it increases the electrostatic energy or is a detriment to other structural factors. The deformation of the spinel structure from cubic to tetragonal is due to the cooperative Jahn-Teller effect. The distorting cations are the Mn^{3+} cations, and their concentration can be modified by oxide-reduction phenomena.

Typical nickel manganite properties

The nickel manganite family of NTC's is known for its exceptional semiconductivity. It crystallizes as an inverse spinel and the degree of inversion decreases with increasing temperature. [1] Additionally, the activation energies of nickel manganites are relatively constant over a wide range of compositions. The combined effect of these factors make this family of NTC's industrially interesting for the production of temperature sensors.

In 1962 Larson *et al.* [16] performed an extensive study into the behavior of nickel manganites, based in part on the work of Verwey *et al.* [17] In general, there is a transition from tetragonal to cubic symmetry as more Ni ions are added to the system, which is driven by the increase of Mn^{3+} ions on B-sites. The increase of Mn^{3+} on B-sites induces stress in the grains of the ceramic, which are then relieved by the appearance of ferroelastic domains. There is a maximum conductivity, at which the conductivity mechanism switches from p-type for Mn-rich compositions, to n-type for Ni-rich compositions (Figure 2.3).

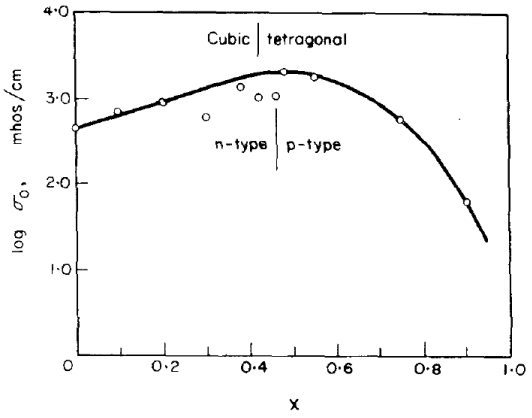

Figure 2.3: 'Infinite temperature' conductivity as a function of the composition for $0 < x < 1$ in $Ni_{1-x}Mn_{2+x}O_4$. [16]

There is still little agreement when it comes to defining the exact valence distribution of the cations in $NiMn_2O_4$. An extensive list of reported cation valence distributions is given in Appendix A, along with the characterization method that was used to measure the distribution. Although certain configurations can account for the magnetic behavior of nickel manganite, they fail to explain the experimental electrical data, which require the coexistence of Mn^{3+} and Mn^{4+} on B-sites.

2.2.2 Electrical properties

The electrical behavior of the nickel manganite family of NTC ceramics is somewhat more complex than in generic semiconductors. In NTCs, and all oxide semiconductors, the concentration of charge carriers is determined solely by the doping level, so the number of charge carriers does not change with temperature. The mobility, μ, decreases with temperature, because as the amount of energy in the system increases, the likelihood of collisions inhibiting net movement also increases. Following this logic, the temperature dependence of the resistivity, ρ, follows from an Arrhenius equation:

$$\rho(T) = \frac{1}{\sigma} = \rho_\infty e^{\frac{E_a}{kT}} \tag{2.2.1}$$

Where:

- σ is the electrical conductivity,
- ρ_∞ is the resistivity at infinite temperature, sometimes referred to as the specific resistivity,
- k is the Boltzmann constant, and
- E_a is the activation energy for electrical conductivity.

In order to be able to use an NTC ceramic for temperature sensing, the activation energy, E_a, must be between 0.15 and 0.5 eV. The value of the specific resistivity of the NTC, ρ_∞, is not quite as important because it can be tailored after the fact by adjusting the geometry of the material. Even so, common values in industry for ρ_∞ range from 1 to 100 MΩ.cm in order to produce temperature sensors with a total resistance on the order of Ω to kΩ at room temperature. [1]

For a piece of NTC ceramic of fixed dimensions (since geometry is such an important factor) and resistivity, (2.2.1) can be simplified to:

$$R(T) = Ae^{\frac{B}{T}} \tag{2.2.2}$$

Where:

- $R(T)$ is the resistance of the NTC at the temperature, T.
- $A = R_\infty$, which is the resistance of the NTC at infinite temperature (ie 1/T=0), and
- B is the 'material constant' of the NTC.

Differentiating (2.2.2) gives the sensitivity coefficient, or temperature coefficient of resistance, of NTCs, α:

$$\alpha = \frac{1}{R} \cdot \frac{dR}{dT} = -\frac{B}{T^2} \tag{2.2.3}$$

Which shows why NTC ceramics have the peculiar property of increased conductivity with increasing temperature. In most spinel thermistors, the B-values will vary from 2000 to 5000 K (see Figure 2.4). This range of B-values subsequently produces room-temperature α values ranging from -2.2 and -5.5 %/K, respectively. [1] The characteristic B-value of a given NTC can be directly calculated from resistance measurements:

$$B = \frac{\ln \frac{R_1}{R_2}}{\frac{1}{T_1} - \frac{1}{T_2}} \tag{2.2.4}$$

Where: R_1 and R_2 are the resistances at the temperatures T_1 and T_2. Normally, R_1 and R_2 are measured at: $T_1 = 25°C$ and $T_2 = 85°C$ or 100°C. Obviously, other temperature ranges are chosen if these temperatures are not relevant to the operational temperature range of the NTC.

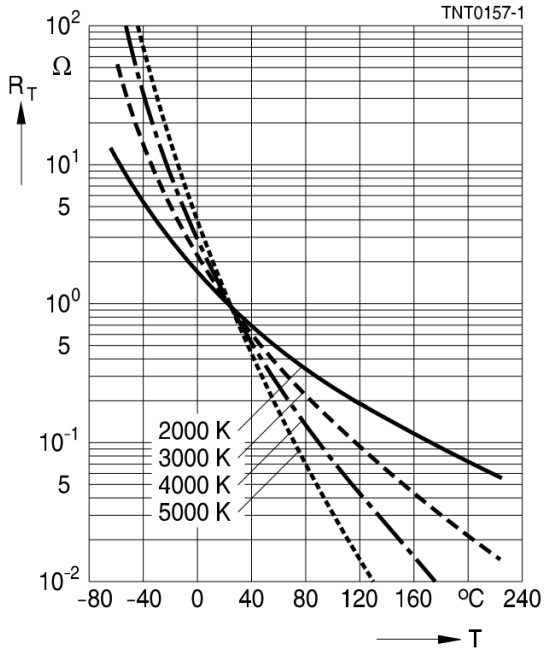

Figure 2.4: Typical resistance/temperature characteristics of NTC thermistors (parameter: B value). [18]

To measure the resistance of an NTC, it must be attached to a measurement circuit that passes an electrical current through it. When a thermistor is used as a temperature sensor, it is assumed that all its characteristics are based on the so-called zero-power resistance, meaning that electric current passing through it does not result in any noticeable temperature increase (self-heating) that may affect accuracy of measurement. [7]

2.2.3 Small polaron hopping conductivity

In oxide semiconductors, electrical conduction occurs via electrons in the conduction band moving from one ion to another. A more precise description of the conduction that takes place in NTC ceramics follows from the 'small polaron hopping' model.

As an electron moves through a solid medium, it induces a potential by repelling negative ions, and attracting positive ions; vice versa for a hole. The combined phenomenon of the charge carrier and its accompanying polarization field is the quasiparticle known as a polaron. The transport of the electric charge can be understood by interpreting it as a lattice vibration (phonon) assisting the jump of charge carriers, among localized states, from one position to another; this is called 'hopping conductivity', and is described by: [19]

$$\sigma = c(1-c)\left(\frac{e^2a^2\nu}{kT}\right)e^{-\frac{E_\mu}{kT}} \tag{2.2.5}$$

Where:

- c and (1-c) are the probability of having, in the case of the manganite family, a Mn^{3+} (donor) or Mn^{4+} (acceptor) ion in an octahedral site, respectively. The quantity c can also be calculated from: $c = n/N$ [20],

- E_μ is the activation energy of the mobility of the charge carriers ($\approx$ 0.49 eV for $NiMn_2O_4$, 0.14-0.79 eV for spinels [21]),
- ν is the phonon frequency ($\sim 10^{13}$ Hz), and
- a is the transport distance.

Small polaron hopping occurs between ions of the same type, but a different valence (like $Fe^{3+} \Longleftrightarrow Fe^{2+}$ or $Mn^{4+} \Longleftrightarrow Mn^{3+}$), which are on equivalent lattice locations. The hopping, and consequent distortion of the octahedra, is illustrated in Figure 2.5 for manganite spinels. The valence of the ions involved may only differ by one unit, if hopping conduction is to take place. The most common ions used for hopping conduction are Mn ions, which have three stable valence states (2+, 3+ and 4+). [11, 16, 22] In spinels, small polaron hopping occurs between ions in the octahedral positions (B-B), because the bond distances, or hopping distances, between ions in tetrahedral sites (A-A and A-B) are larger.

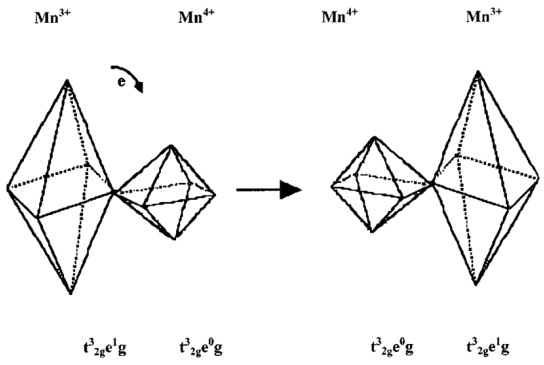

Figure 2.5: Scheme of electron jump between two manganese ions in a manganite spinel. [22]

Small hopping conduction is distinguishable from other kinds of conduction by two characteristics: [23]

1. a thermally activated charge mobility, E_μ, and
2. a temperature independent Seebeck coefficient (at a fixed deviation from the stoichiometry).

The mobility of the charge carriers is typically low, orders of magnitude lower than for normal band-conduction which is around $\approx 0.1 cm^2/Vs$. It has been reported to range from 10^{-4}-10^{-2} cm^2/Vs for iron aluminate spinels [23] or 10^{-5}-10^{-8} cm^2/Vs at 25°C for nickel manganite spinels. [24] When hopping conductivity occurs, the mobility of the electrons, μ, is thermally activated with an energy E_μ, and can be calculated from: [20]

$$\mu = \frac{B}{T} e^{\frac{-E_\mu}{kT}} \tag{2.2.6}$$

Mobility is generally measured using the Hall effect, but since the mobility in these materials is so low, it is difficult to interpret or even make Hall effect measurements. Thermoelectric measurements

are not burdened by this problem, and are therefore preferred for determining the conductivity of spinels. [20]

The thermopower of a material is used to describe the temperature dependence of the material's conductivity. Applying a temperature difference over the thickness of a material induces its charge carriers to move from the hot to the cold side; the thermopower is the magnitude of the thermoelectric voltage in response to this temperature difference. The Seebeck coefficient, Q, quantifies the thermopower of the material, which for broadband semiconductors is given by: [23]

$$Q = \pm\frac{k}{e}\left[\frac{E_F}{kT} + A_s\right] \tag{2.2.7}$$

Where:

- E_F is the Fermi energy with respect to the conduction level, and
- A_s is a constant which depends on the specifics of the scattering mechanism.

In broadband semiconductors, Q is strongly dependent on the temperature, as (2.2.7) shows. However, for small-polaron hopping conduction the number of charge carriers can be assumed to be fixed, which means that the entropy transported per charge carrier, S_T, will also be fixed. As a result of this constant entropy, the thermopower becomes temperature independent. Assuming that only one charge carrier will be allowed on any given site, and that all other interaction effects are negligible, Heikes [25] developed a new formula for a temperature independent Seebeck coefficient:

$$Q = \pm\frac{k}{e}\left[\ln\beta\left(\frac{1-c}{c}\right) + \frac{S_T}{K}\right] \tag{2.2.8}$$

Where:

- β is the degeneracy factor involving the spin and the orbital degeneracy of the electronic carrier, and
- S_T is the vibrational entropy associated with the polaron environment ($\approx 10\mu V/K$) [23].

The sign of Q shows whether the hopping conductivity taking place in the NTC is p- or n-type, although this method may not be entirely valid. The transition from n $\rightarrow$ p transition that (2.2.8) predicts occurs at high electron concentrations (for $S_T = O$) when: [20]

$$c = \frac{\beta}{1+\beta} \tag{2.2.9}$$

At high values of c ($\geq$ 0.1), (2.2.8) is no longer valid, as a consequence of interaction effects and oxygen vacancies which affect the conductivity.

There is a great deal of controversy on which type of conductivity is dominant for nickel manganite spinels. Subsequently, there has been much research into finding the carrier type and the exact cation valence distribution (shown in Table A.1). Reported Seebeck measurements for the Ni-Mn-O family are given in Table 2.1.

Table 2.1: Conduction types reported for nickel manganite spinels.

Year	Investigators	Composition	Carrier type	Temperature range [°C]
1962	Larson *et al.* [16]	$Ni_xMn_{3-x}O_4$ (x >0.54)	n	-190 to 425
		$Ni_xMn_{3-x}O_4$ (x <0.54)	p	
1969	Kshirsagar [26]	$NiMn_2O_4$	n	50 to 400
		Cu-Ni-Mn-O	p	
		$CuMn_2O_4$	p	
		Cd-Cu-Mn-O	p	
		$CdMn_2O_4$	p	
1980	Suzuki [27]	Cu-Co-Ni-Mn-O	p	-115 to 20
1981	Metselaar *et al.* [28]	Mn_3O_4	p	900 to 1400
1982	Brabers and Terhell [29]	$NiMn_2O_4$	n	25 to 350
		$NiMnZnO_4$	p	
1988	Dorris and Mason [21]	Mn_3O_4	p	900 to 1500
		$NiMn_2O_4$	n	350 to 600
		$CuMn_2O_4$	p	725 to 975
1991	Gillot *et al.* [30]	$Ni_{0.57}Mn_{2.43}O_4$	n/p	25 to 525
		$Ni_xMn_{3-x}O_4$ (x >0.60)	n	
1991	Sasamoto *et al.* [31]	Fe-Co-Ni-Mn-O	p	200 to 500
1994	Topfer *et al.* [32]	$NiMn_2O_4$	n	20 to 160
		$Li_{1/3}NiMn_{5/3}O_4$	n	
		$Li_{1/6}NiMn_{11/6}O_4$	n	
		$FeNiMnO_4$	p	
		$Zn_{0.1}Fe_{0.9}NiMnO_4$	p	
		$Cu_{1/3}NiMn_{5/3}O_4$	p	
		$Cu_{2/3}NiMn_{4/3}O_4$	p	
2001	Groen *et al.* [24]	Fe-Ni-Mn-O	p	Room temperature

As Table 2.1 indicates, at high nickel contents, the Ni-Mn-O system is dominated by n-type conductivity, while all other types of nickel-manganites experience p-type conductivity. Perhaps the discrepancy found in the charge carrier type of high Ni% nickel-manganites is due to the method used to calculate the Seebeck coefficient.

Through hopping conduction, it becomes clear why substituting stable trivalent ions for Mn^{3+} decreases the conductivity in NTC ceramics. A lower amount of available Mn^{3+} ions directly translates to less Mn^{3+}/Mn^{4+} pairs available for hopping. Additionally, NTC ceramics that have been cooled in air after sintering will experience a similar depletion of Mn^{3+}. In this case, the depletion of charge carriers does not take place by substitution, but by oxidation of the Mn^{3+}.

2.2.4 Stability

Over time, most electroceramics experience a decrease in their properties even though they are not subjected to external electrical or mechanical stresses, or changes in temperature. In NTC's, this 'aging' is ascribed to a redistribution of the charge carriers, whatever the cause may be. Aging is quantified via a calculation of the thermometric drift, DR/R, at each time interval using the following equation:

$$\frac{\Delta R}{R} = \frac{(R_{current} - R_{initial})}{R_{initial}} \cdot 100 \tag{2.2.10}$$

The initial change in resistance is severe, but slowly levels off over time. Aging can be accelerated, allowing the properties of the NTC to stabilize before use as a temperature sensor, by heating to temperatures above room temperature, but below the decomposition temperature of about 200°C. Pre-aging NTC's normally stabilizes the properties after 500 to 1000 hours at increased temperature (Figure 2.6). After this pre-aging, the resistance of the NTC will increase only slightly when exposed to typical environmental and electrical stresses (Figure 2.7).

The stability of NTC ceramics is commonly agreed to be dependent on: changes in the chemical composition of the NTC, cation rearrangements in the crystal structure, and interactions at the electrode-ceramic interface. [33, 34] Fritsch *et al.* [35] showed that the severity of aging also depends on the thermal history of the NTC, and that in general, quenched NTC's tend to show lower levels of aging when compared to ones that have been slow-cooled. [36]

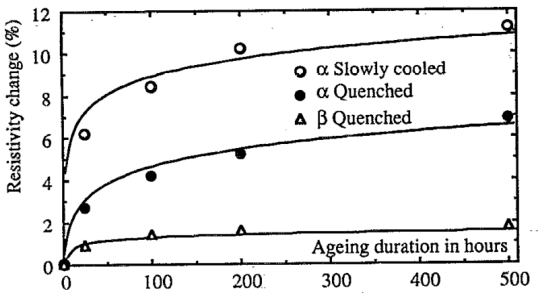

Figure 2.6: Typical resistance drift for quenched and slow cooled NTC's at 125°C. [36]

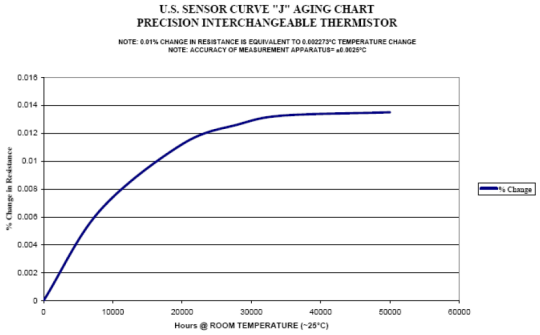

Figure 2.7: Typical resistance drift at room temperature for NTC's, after pre-aging.

Cause of aging

Even though there is some consensus as to what affects the stability of NTC's, the exact cause of the aging remains unclear. Starting in the 1990's, there has been a great deal of research aimed at understanding the origin of the instabilities. [22, 24, 35–49]

Castelan *et al.* [36] proposed in 1992 that aging in $Mn_{7/3-x}Ni_{2/3}Cu_xO_4$ is caused either by the gradual migration of Cu^{2+} from tetrahedral to octahedral sites or by the migration of Ni^{2+} from octahedral to tetrahedral sites over time. They concluded that the amount of octahedral pairs that are capable of forming small polaron hopping paths for conduction plays a large role in the stability of NTC's.

Regardless of the theory applied to explain aging, there is a clear consensus that aging is indeed a function of the ratio of the octahedral pairs forming conduction paths. It is commonly agreed to be a consequence of the redistribution of charge within the NTC over time, and the cause of this charge redistribution is explained through the following three phenomena:

1. a change in the degree of inversion, γ, due to cation migration over time,
2. the formation of Mn^{3+} clusters on octahedral sites, and

3. the diffusion of cation vacancies as a consequence of preferential reoxidation at the grain boundaries, after cooling down from sintering temperatures in air.

Charge redistribution

Fritsch *et al.* [35] proposed in 1998 that oxide-reduction phenomena reduced the amount of hopping pairs at octahedral sites and cited this as the cause of aging in NTC's. They found that almost no aging occurred in $Ni_{0.73}Mn_{2.27}O_4$ ceramics that had been metalized in nitrogen, even though the ceramics metalized in air experienced a considerable amount of aging.

The cationic distribution in nickel manganite spinels is highly dependent on the cooling rate after sintering. [50, 51] Therefore, any metalization process like the one Fritsch *et al.* [35] executed involving a heat treatment at 800°C to 900°C will affect the distribution of cations, in this case transferring Ni^{2+} from octahedra to tetrahedra. As a result of annealing the nickel manganites at 850°C they also found 'coffee bean'-shaped precipitates of 20 to 40 nm (Figure 2.8), which they determined to have been caused by oxidation. Once the samples with the coffee bean like precipitates were aged, the precipitates disappeared. In 1997, Battault *et al.* [37] also found a correlation between the microstructure of NTC's and the severity of aging. As a result of the disappearance of the precipitates and the minimal aging in nitrogen, they concluded that aging in NTC's is caused by the reduction of hopping pairs, due to the diffusion of vacancies to the surface of the ceramic.

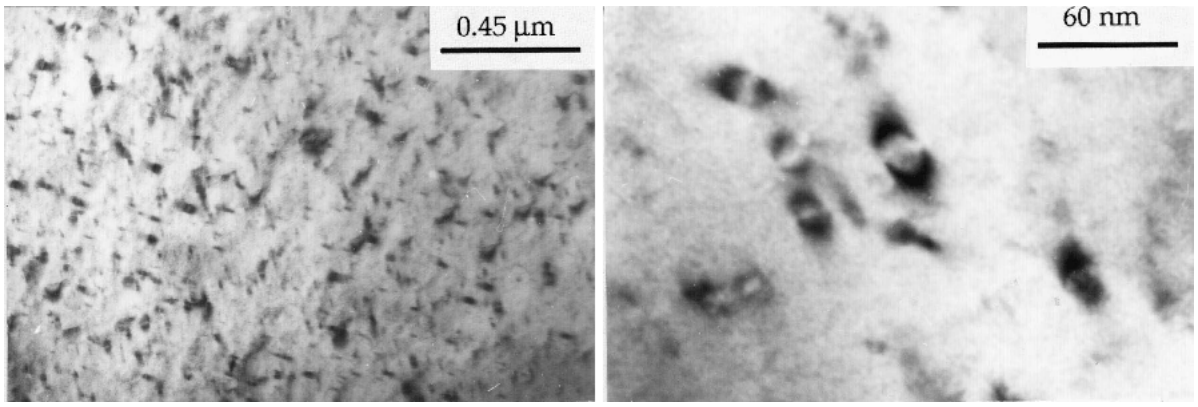

Figure 2.8: TEM micrograph of $Ni_{0.73}Mn_{2.27}O_4$ ceramic sintered at 1160°C in air, slow cooled (-6°C/h), and metalized (annealed at 850°C, cooled at -55°C/min). [35]

There has been extensive research over the years to corroborate the cation redistribution model, and that there is indeed a change of the degree of inversion in NTC's over time. Wang *et al.* [38] used the model to explain the aging in $Fe_xMn_{2.34-x}Ni_{0.66}O_4$ ($0<x<1$) ceramics, in which Fe^{3+} ions migrate from octahedra to tetrahedra. As did Battault *et al.*[1998] [41] with $Mn_{3-x}Fe_xO_4$ NTC's. Metzmacher *et al.* [40], in accordance with the cation redistribution model, proposed that aging could be reduced by ferroelastic pinning of Mn^{3+}, which would inhibit the movement of the cations, and subsequent charge redistribution between tetrahedra and octahedra. Incidentally, the cation redistribution model is also supported by the fact that perovskite NTCs are inherently more stable than their spinel counterparts, since cation transfers from A to B are highly unlikely in perovskites. [1]

Metz *et al.* [22] found that tetragonally distorted $Ni_xMn_{3-x}O_4$ ceramics with low Ni content experienced more severe aging. They proposed a decomposition mechanism in which localized regions of

higher Mn^{3+} cation concentration, referred to as clusters, form while heating the NTC. They attribute the tendency of Mn^{3+} to cluster to the Jahn-Teller distortions of octahedral sites and the decrease of the degree of inversion due to heating. This increases the site preference of Mn^{3+} for octahedra, forcing the Mn^{3+} cations into B-sites to decrease the energy of the system. When this clustering occurs, Ni^{2+} ions are displaced, and moved into the energetically unfavorable tetrahedral sites. Ni^{2+} also has a strong B-site preference, and over time the driving force becomes too great; the Ni^{2+} move into octahedral positions, resulting in a transformation of the crystal structure from spinel to rock salt.

Small areas of the NTC still contain enough Mn to maintain a spinel structure, and this results in the formation of little spinel-islands in the rock-salt structured matrix, which over time (and with sufficient temperature) will regrow together to form complete grains. This explains why more aging is observed in tetragonal spinels than in cubic spinels.

Fang *et al.* [39] also took note of this decomposition mechanism in $NiMn_2O_4$. They concluded that the formation of a rock salt phase was driven by the strong octahedral site preference of the Ni^{2+} cations. Electrical measurements of slow-cooled NTC's compared with single phase samples, after several hours at 400°C, show that a reversal of the decomposition described above results in a change of the resistance of the material, due to a change in Ni^{2+} concentration in the spinel phase. [39, 49]

Oxidation of grain boundaries

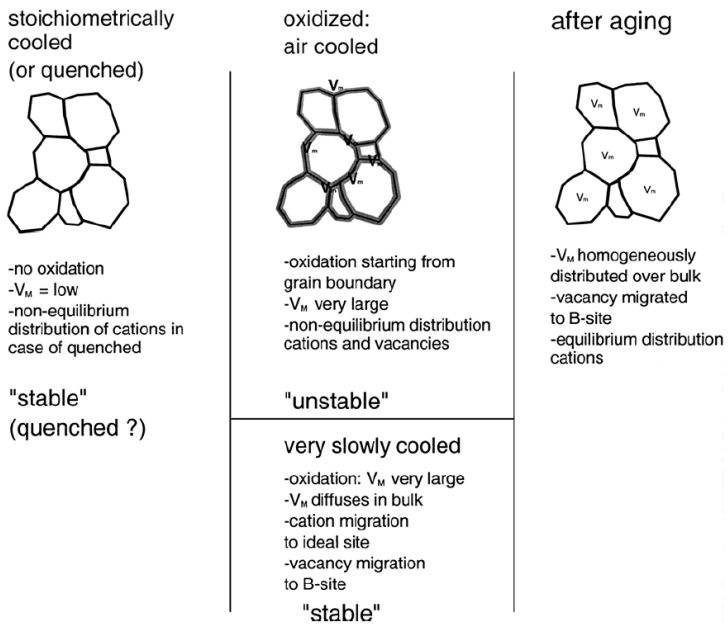

Figure 2.9: Schematic presentation of the processes which occur during cooling and aging of NTC ceramics. [42]

Groen *et al.* [24, 42] proposed a model that states that aging in NTC's is a consequence of cation and vacancy rearrangement, due to oxidation of the grain boundaries during cooling after sintering (Figure 2.9). Their model was based on findings from magnetic measurements, AC impedance and Seebeck measurements. What the model proposes, is that the act of stoichiometrically cooling or quenching NTC ceramics suppresses the reoxidation of grain boundaries. Yet, when an NTC is slow-cooled in air, reoxidation will preferentially occur at the grain boundaries, in a process given by:

$$\frac{1}{2}O_2 \Longleftrightarrow O_0^x + \frac{1}{4}V_A^{II} + \frac{1}{2}V_B^{III} + 2p^\bullet$$

Ceramics that are left to slow-cool will maintain a high temperature for a longer period of time than quenched, or stoichiometrically cooled ceramics. At high temperatures, cation vacancies that are formed at grain boundaries tend to diffuse inside the grains. When this happens, the cation vacancies move into B-sites, since they have a thermodynamic preference for octahedral interstitials. The increase of B-site vacancies results in an overall increase of resistivity, since the B-B conduction is now somewhat inhibited, and an increase in electrical drift.

Wang *et al.* [38] investigated the effects of annealing and cooling on the aging of NTC's in both air and nitrogen for the specific composition of: $Fe_{0.5}Mn_{1.84}Ni_{0.66}O_4$. Their findings are in line with Groen *et al.*'s [42] model.

Compositional purity and its effect on aging has also been examined in some detail, and the results are contradictory. Gyorgyfalva *et al.* [43] found that, on the whole, single phase ceramics experience less aging than multi-phase ceramics. Vakiv *et al.* [47] and Shpotyuk *et al.* [46, 48] observed that the effects of aging all but disappear in ceramics that contain a small amount of NiO as a second phase.

Through the brief introduction on the crystal structure, electrical properties, and stability of nickel manganite NTC's presented here, it becomes clear that there are still many aspects of NTC's under investigation. How the thermal history and composition of NTC's affects their stability over time will be investigated in the following chapter.

CHAPTER 3

RESULTS

In nickel manganite negative temperature coefficient of resistance (NTC) ceramics, the resistivity and characteristic B-value are dependent not only on the chemical composition, but also the sintering scheme. An example of these variations in electrical properties, solely due to differences in preparation and composition, is given in Figure 3.1 for the resistivity and Figure 3.2 for the B-value for $Ni_xMn_{3-x}O_4$ with increasing nickel content.

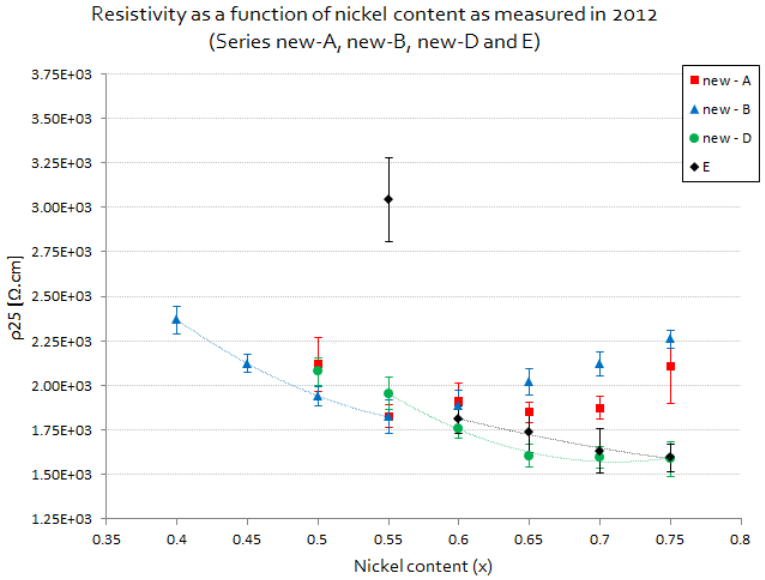

Figure 3.1: Resistivity at 25°C of newly sintered reference series (new-A), quenched series (new-B), post-annealed series (new-D) and slow cooled series (E), for all eight compositions of $Ni_xMn_{3-x}O_4$ for $0.4 < x < 0.75$. Note: Each data point of these graphs represents the average electrical properties of 5 to 7 samples, while the error bars show the standard deviation. Resistivity values at low nickel contents are not shown since they are at the much higher values of $10^4\Omega$.cm. Trendlines are between the compositions which consist of a single phase spinel.

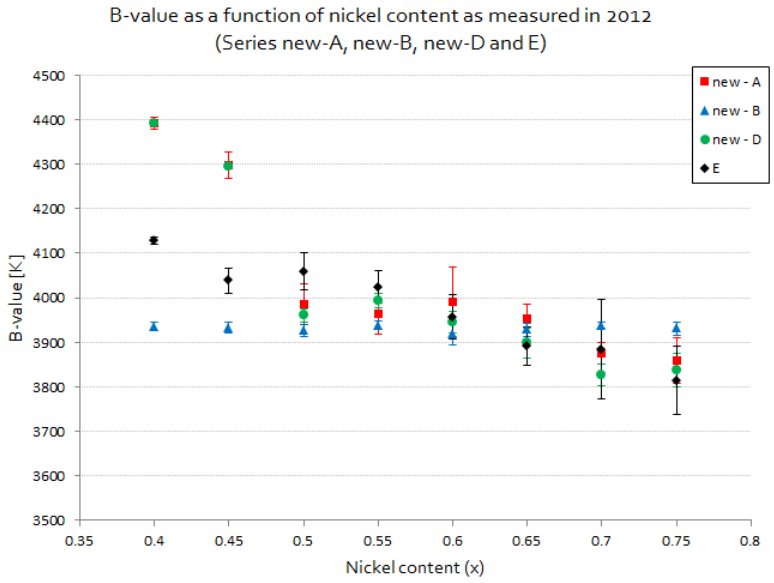

Figure 3.2: B-value of newly sintered reference series (new-A), quenched series (new-B), post-annealed series(new-D) and slow cooled series (E), for all eight compositions of $Ni_xMn_{3-x}O_4$ for $0.4 < x < 0.75$.

Each series shown in Figure 3.1 and 3.2 was heated and sintered at the same rate and temperature and for the same amount of time. The only difference is the cooling rate applied for each NTC series. Differences in time spent at high temperature and exposure to oxygen during cooling naturally have an effect on the ultimate properties of the NTC ceramic, just as they do for any generic ceramic or metal. It follows that the stability of the electrical properties is also dependent on the cooling rate and composition. In this chapter, both the phase formation and stability of nickel manganite NTC ceramics is studied.

The microstructural consequences of differences in cooling rate and composition will be analyzed in section 3.3. Additionally, the effect of room temperature aging, and stability, of these nickel manganite ceramics will be investigated through an aging study of both long-term room temperature aged ceramics and freshly sintered ceramics (section 3.4). First, the preparation methods and measurement setup will be described in section 3.1.

3.1 Preparation of NTC ceramics

NTC ceramic pellets from the $Ni_xMn_{3-x}O_4$ composition for nickel contents of $0.4< x <0.75$, manufactured in 2000, were used for this research. The NTC pellets were thoroughly characterized after sintering in 2000; the resistance (R_{25} and R_{85}) and density of each pellet was measured, and in-situ high temperature x-ray diffraction (XRD) of each composition was performed. Additional thermal gravimetric analysis (TGA) measurements of a number of samples were also performed. After characterization, the NTC pellets were allowed to age at room temperature until 2012.

The eight different compositions within the $0.4< x <0.75$ range have each been designated by a code for simplification from p530 for the lowest nickel content compositions, up to p537 for the highest nickel content compositions.

Green pellets of each of the eight compositions were prepared according to four different preparation schemes in 2000. These sintering schemes are referred to as:

A – Reference
- Heated in air at 120 K/h
- Sintered for 6 hours at 1250°C
- Cooled in air at 300 K/h

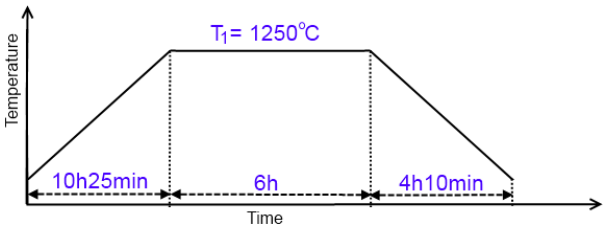

B – Quenched
- Heated in air at 120 K/h
- Sintered for 6 hours at 1250°C
- Quenched in air

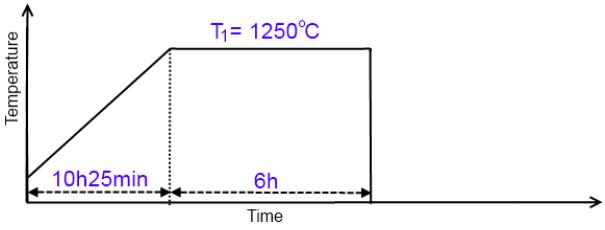

C – Stoichiometrically cooled
- Heated in air at 120 K/h
- Sintered for 6 hours at 1250°C
- Stoichiometrically cooled
- Note: Sintering occurred in air, while during cooling a controlled atmosphere (O_2/N_2) was used to prevent oxidation of the ceramic.

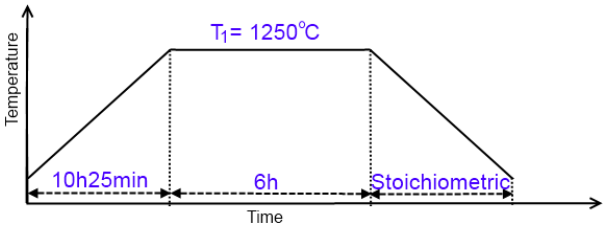

D – Post annealed
- Heated in air at 120 K/h
- Sintered for 6 hours at 1250°C
- Cooled in air at 300 K/h
- Annealed for 100h in air at 1000°C.
- Cooled in air at 30 K/h.

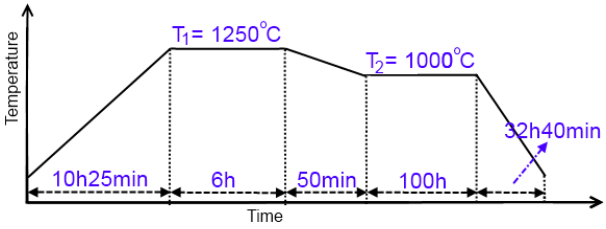

Of each sintering scheme A-D, two kinds of pellets were manufactured in 2000:

- 20 sintered pellets of approximately 5.4mm diameter and 0.9mm thickness, and
- 18 sintered pellets with electrodes applied through vacuum metalization, with an electrode diameter of 4.6mm.

To study the effect of room temperature aging from 2000 to 2012 of these pellets, unaged samples of the same composition and heat treatment were desired. To that end, green pellets from each composition (p530-p537) were sintered according to sintering schemes A,B and D. It was not possible to recreate the conditions required for stoichiometric cooling. The newly sintered series are referred to as 'new-A', 'new-B' and 'new-D'.

A fifth sintering scheme (named series E) was applied to the green pellets (of all eight compositions) according to the slow cooling scheme commonly used in the work of Fritsch *et al.* [35]:

E – Slow cooled
- Heated in air at 120 K/h
- Sintered for 6 hours at 1250°C
- Cooled in air at 6 K/h.

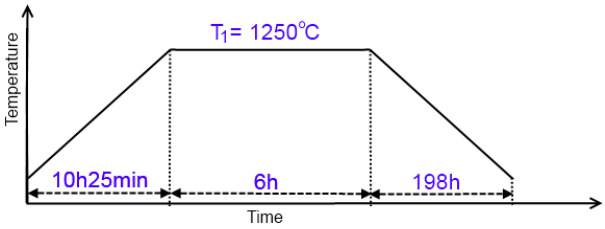

The resistance measurements in 2012 were taken with a Phillips PM2525 multimeter. To ensure the resistance was measured at the correct temperature, the NTC pellets were dipped in a UB20 Lauda oil bath controlled by a R400 Lauda temperature controller, which were both certified to have an accuracy of ± 0.05°C. XRD diffractograms were measured with a D4 Endeavor, using Cu-K_α. Scanning electron microscope (SEM) micrographs were taken with a JEOL JSM-6510LV SEM.

3.2 Varying sintering length and temperature

In order to investigate the effect of sintering time and pressure on the conductivity of the sintered ceramics, identical pressed NTC pellets of composition $Ni_{0.6}Mn_{2.4}O_4$ (p534) are subjected to eight different variations of sintering scheme A (shown in Figure 3.3). In 2000, these same pressed pellets were sintered for six hours at 1250°C and allowed to cool according to differing methods (A-D). In this case, the pressed pellets are sintered at differing temperatures, for different lengths of time, and allowed to cool according to the same method. Sintering temperatures of 950°C, the calcination temperature which results in a single phase spinel at this composition, 1050°C, 1150°C and 1250°C are compared to one another, as well as sintering lengths of 30 minutes and 6 hours.

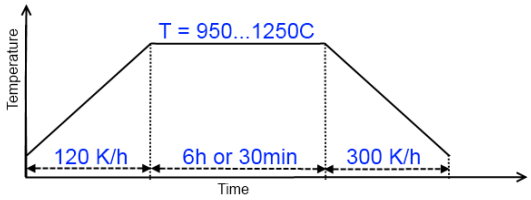

Figure 3.3: Sintering scheme applied for pressed NTC NiMn pellets from the calcination temperature of 950°C increasing incrementally until the sintering temperature of 1250°C.

All the sintered NTC pellets have attained resistivities in the range of 10^3 Ω.cm (Figure 3.4), regardless of the sintering length or temperature. Sintering at 1250°C for both 30 minutes and 6 hours and 1150°C for 6 hours results in the lowest resistivities. The NTC pellets sintered for 30 minutes at 1150°C have a higher resistivity than those at both 1050°C and 1250°C with the same sintering length. In general, as the sintering temperature and length are increased, the resistivity decreases.

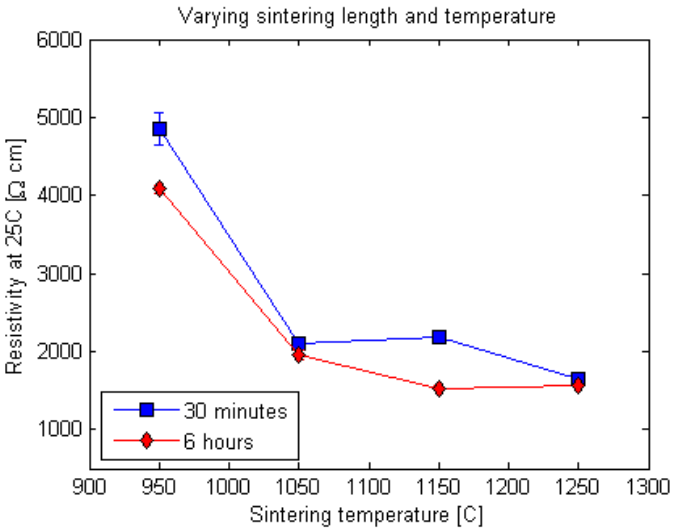

Figure 3.4: Resistivity at 25°C of the eight different types (950,1050,1150, and 1250°C sintered for 30min and 6h) of NTC ceramic pellets.

3.3 Microstructural analysis

In order to study the phases formed in nickel manganite NTC ceramic pellets as a function of composition and cooling scheme, extensive analysis with SEM was performed on the room temperature aged NTC series A-D. The cross-section of each NTC pellet was imaged in backscattered electron composition (BEC) mode to best visualize a second phase, if there would be any. The SEM micrographs, shown in Figure 3.5, were ordered according to their approximate position along the phase diagram, assuming the quenched series represents a frozen image of the microstructure at the highest temperatures, and the post annealed series - the slowest cooled of the four - represents the effect of oxidation experienced during cooling to lower temperatures in air.

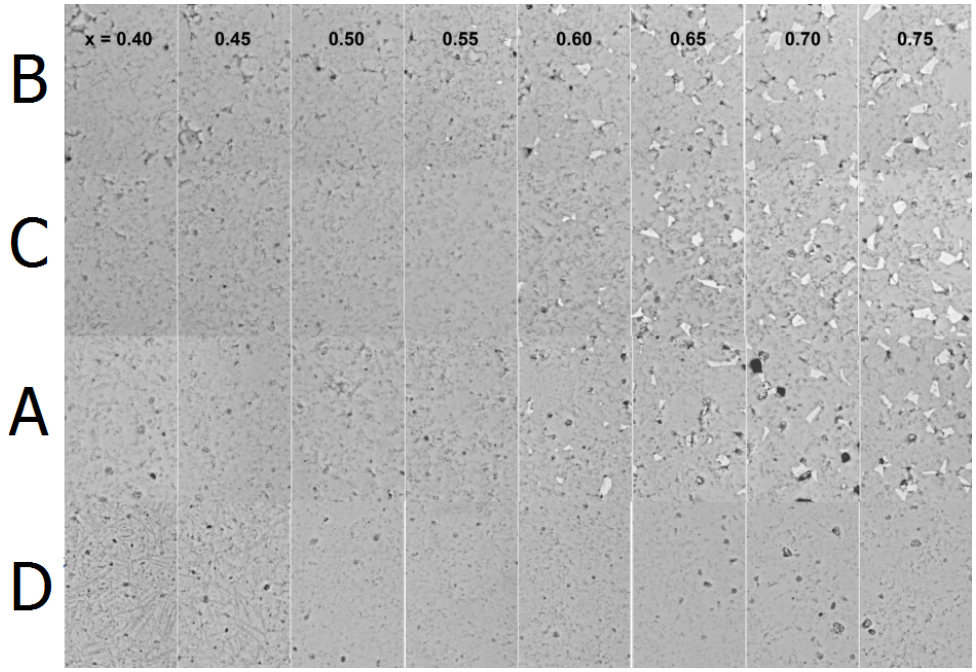

Figure 3.5: SEM micrographs of the cross-section of the pellets of series A-D for all compositions $0.4 < x < 0.75$, $Ni_xMn_{3-x}O_4$ taken in 2012 in BEC mode at 500x magnification. From top to bottom, the images show sintering schemes: B - C - A - D.

Most of the series appear to consist of a single phase; whether that phase is a cubic or tetragonal spinel is not evident from SEM. The upper right hand portion of the composite SEM micrograph shows the segregation of a NiO second phase in the form of lighter white patches, as compared to the spinel Ni-Mn-O matrix. The lower left hand corner shows the segregation of a small splinter-like, and darker, Mn-O second phase. This phase is only apparent for the series: 530A, 530D, and 531D.

3.4 Aging study

To investigate the effect of long-term room temperature aging on the electrical properties of nickel manganite NTC ceramics, an aging study was performed on both the aged samples, and newly sintered green samples. NTC samples from each composition, age, and sintering scheme were aged for a period of a total of 33 days at 125°C. The R_{25} of each sample of series A-D was measured after: 1, 2, 5, 8, 16 and 33 days. Due to time constraints, the R_{25} of new-A, new-B, new-D and E could only be measured on day: 1, 2, 5 and 21. The resistance drift, DR/R, at each time interval was calculated from Eq. (2.2.10).

3.4.1 Resistance drift at final aging step

After 33 days at 125°C, the original A-D series show almost no aging. The aging of all four series is shown in Figure 3.6 and 3.7 as a function of nickel content per sintering scheme.

The DR/R measured for both the B series (quenched) and C series (stoichiometric) falls within the ±0.4% error of the oil bath, and can therefore be said to have experienced no aging effect from the time spent at 125°C. The DR/R of the A series (reference) of most compositions is also within the error of the oil bath, except for nickel contents of 0.5 and 0.55, which age negatively at ≈ -1.0%.

The DR/R of D series (post annealed) is slightly larger, and is not negligible. The average aging of the D series is ≈ -1.0%, except for the same compositions of nickel contents 0.5 and 0.55.

After 21 days at 125°C, the new A,B and D as well as the E series all show signs of aging. The aging of these four series is shown in Figure 3.8 as a function of nickel content per sintering scheme.

The DR/R measured for both the new-B series (quenched) ages slightly, with a positive change in resistivity of ≈ 2%. The new-D series (post annealed) ages between ≈ +1% to ≈ -3%, depending on the composition.

The DR/R of the new-A series (reference) and E series (slow cooled) is somewhat erratic. The changes in both series are extreme for nickel contents of 0.6, making it likely there is some problem with this composition of NTC pellets. The positive aging of the slow cooled E series is expected, while the negative aging of the new-A series is not.

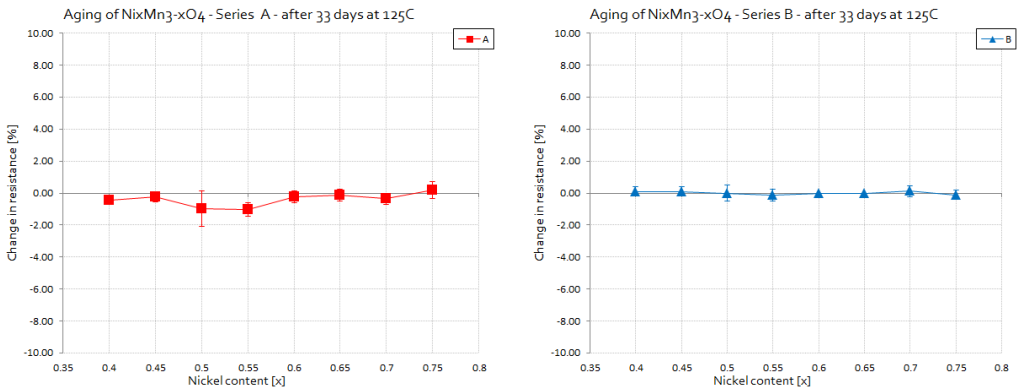

(a) Reference samples (A-series) **(b)** Quenched samples (B-series)

Figure 3.6: Resistance drift after 33 days at 125°C of $Ni_xMn_{3-x}O_4$, for $0.40 < x < 0.75$, for sintering schemes series A and B.

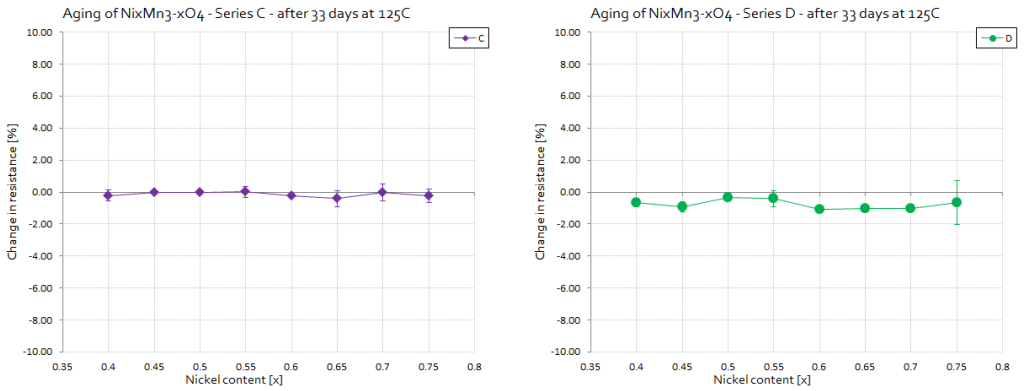

(a) Stoichiometrically cooled samples (C-series) **(b)** Post annealed samples (D-series)

Figure 3.7: Resistance drift after 33 days at 125°C of $Ni_xMn_{3-x}O_4$, for $0.40 < x < 0.75$, for sintering schemes series C and D.

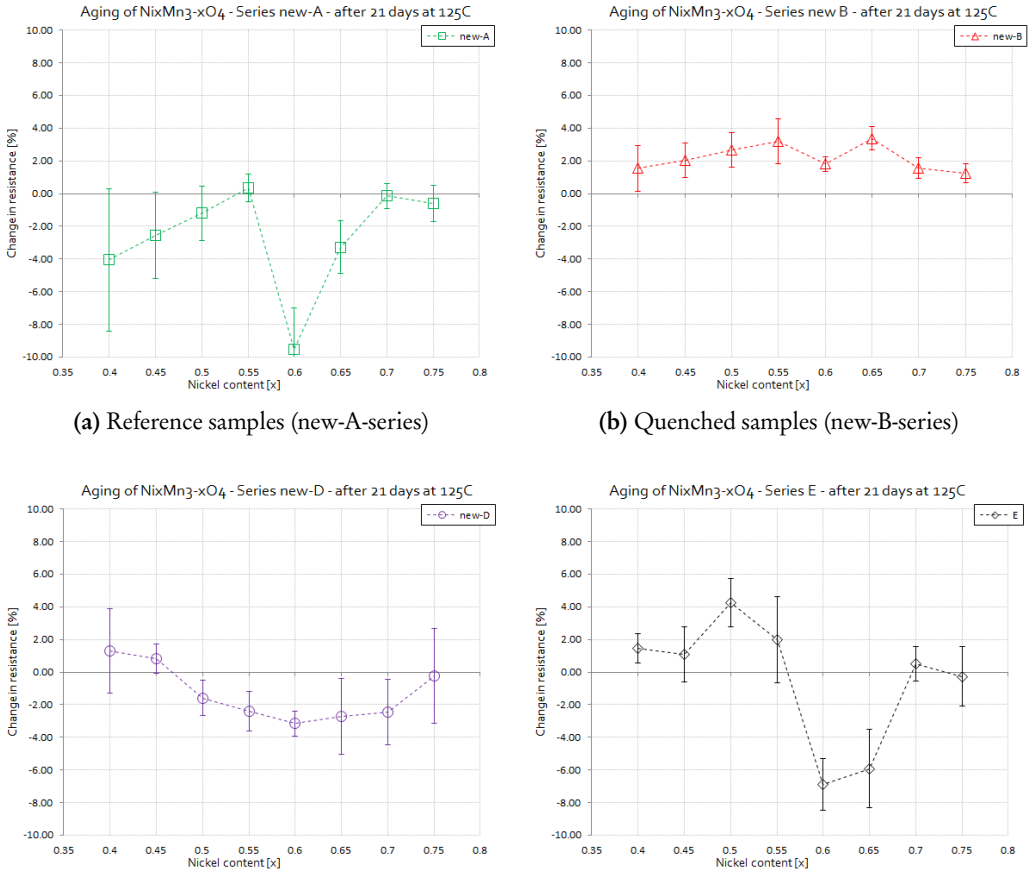

(a) Reference samples (new-A-series) **(b)** Quenched samples (new-B-series)

(c) Post annealed samples (new-D-series) **(d)** Slow cooled samples (E-series)

Figure 3.8: Resistance drift after 21 days at 125°C of $Ni_xMn_{3-x}O_4$, for $0.40 < x < 0.75$, for sintering schemes series new-A, new-B, new-D and E.

3.4.2 Resistance drift after five days

The resistance drift of all NTC samples after five days at 125°C is used to compare the properties of the original A-D to the newly sintered series. The calculated DR/R at day five is shown per sintering scheme, as a function of nickel content in Figure 3.9 and 3.10. The measurement at day five was chosen, since this can be compared to the data collected for new-A, new-B, new-D and E, and since the most drastic changes in resistance will have already taken place by day five.

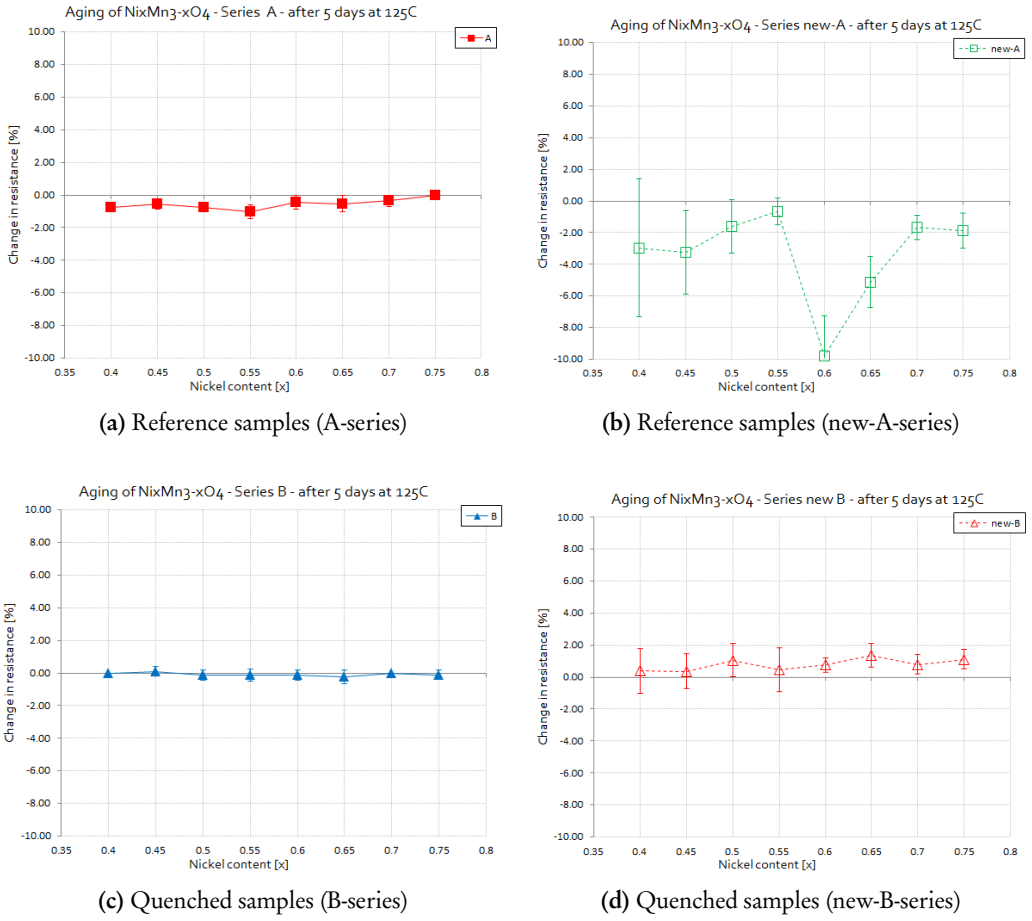

(a) Reference samples (A-series)

(b) Reference samples (new-A-series)

(c) Quenched samples (B-series)

(d) Quenched samples (new-B-series)

Figure 3.9: Resistance drift after five days at 125°C of $Ni_xMn_{3-x}O_4$, for $0.40 < x < 0.75$, for sintering schemes series A, new-A, B and new-B.

The aging of both the original A, B and new-A, new-B series is shown in Figure 3.9, while the aging of D, new-D, C and E are shown in Figure 3.10, as a function of nickel content per sintering scheme.

Similar to the results at the final aging step, after five days of aging the B series shows almost no effects of aging, while the A series has aged negatively at ≈ -1.0% (Figure 3.9). The counterpart to B, the new-B series, shows positive aging as anticipated, on the order of 1.5%. The new-A series has also aged negatively, but behaves unlike its counterpart, A. Again, at nickel contents of 0.60 and 0.65, extreme changes in resistance are evident and these changes are not in line with those measured at the other compositions. Perhaps there was a problem with this composition of green NTC pellet, since all compositions were sintered together in the same furnace at the same time.

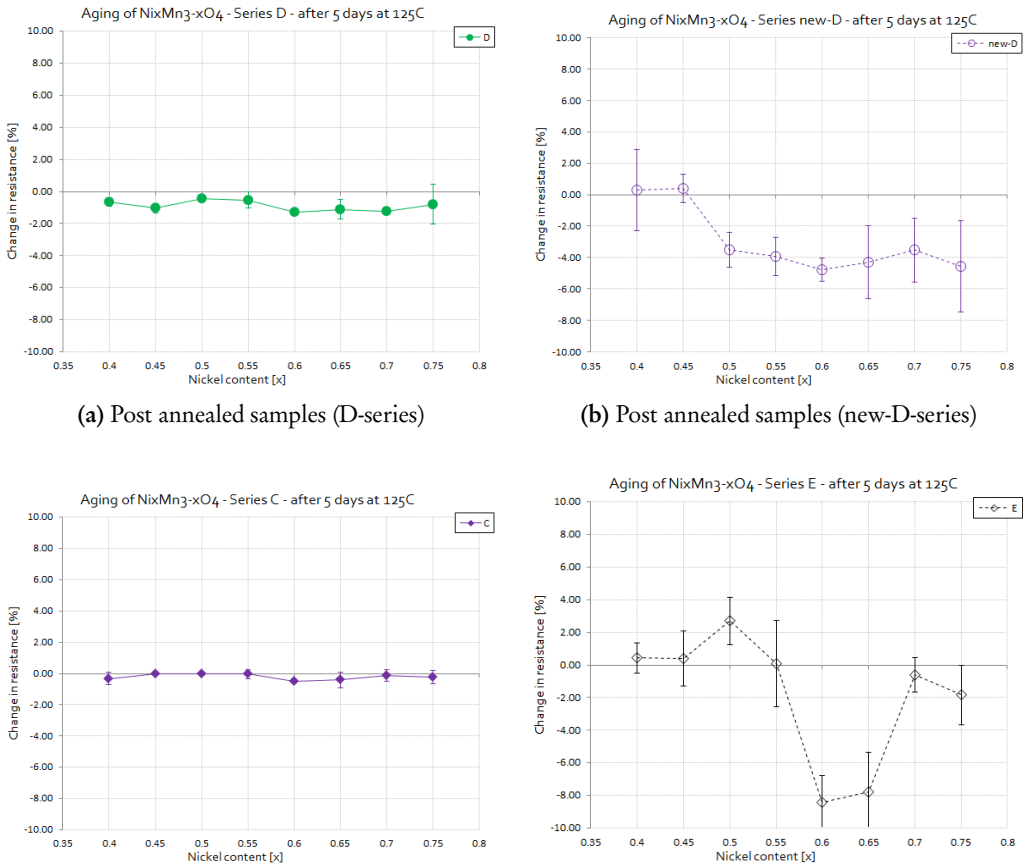

(a) Post annealed samples (D-series)

(b) Post annealed samples (new-D-series)

(c) Stoichiometrically cooled samples (C-series)

(d) Slow cooled samples (E-series)

Figure 3.10: Resistance drift after five days at 125°C of $Ni_xMn_{3-x}O_4$, for $0.40 < x < 0.75$, for sintering schemes series D, new-D, C and E.

The aging behavior of the D and new-D series is also not entirely unlike what was shown previously at the final aging step (Figure 3.10). The change in resistance of D appears to be negative, but consistent, at ≈ -1.0%. The aging of new-D after five days of aging is higher than at the final aging step, and for most compositions lies at ≈ -4.0%.

The stoichiometrically cooled series C does not appear to be affected by aging after five days at 125°C, and while this is true for some of the slow cooled (E) compositions, there are some major discrepancies (see Figure 3.10). Just like the new-A series, at nickel contents of 0.60 and 0.65, the slow cooled series has experienced extreme aging. Again, it is more likely that these outliers could be ascribed to problems during production or sintering of the samples. New samples have been prepared at both compositions, but due to time constraints have not yet been tested. The other slow cooled compositions age between +2% and -2%.

CHAPTER 4

DISCUSSION

4.1 Electrical properties and stability

The stability of nickel manganite NTC ceramics, much like their other electrical properties, depends on the cooling conditions applied in their preparation, as well as their composition. The temperature and length at which these negative temperature coefficient of resistance (NTC) ceramics are sintered does have an effect on the electrical properties of the sintered ceramic, but it is not nearly as significant as the cooling conditions (Figure 3.3).

Overall, the long-term room temperature aged NTC ceramics are more stable than the newly sintered NTC ceramics, as one would expect.

The change in resistivity of the new A series is clearly different from that of the original A series. The new A series has aged negatively which is unexpected and unsupported in literature. The difference between the aging behavior of the original and new A series is not wholly unexpected, since the formed phases in the new A series are not identical to the original A. Therefore, the results of the aging study of the two A series can not be compared to one another.

The new B series ages slightly, with a positive change in resistivity of $\approx 1.5\%$. When compared to the results of a similar aging experiment reported in Dr. Fritch's doctoral thesis [52] (shown in Figure 4.1), the change in resistivity measured for the new-B series appears to follow the same trendline. The similarity of results between the two aging studies would seem to validate the results of this aging study. Comparing the aging of the new and original B series, the effect of long term room temperature aging on the electrical properties of the original B series seems to be clear: The new B series ages (slightly) while the original B series does not, so one can conclude that over time the original B series has reached an equilibrium state.

The measured aging of the new D series, unlike the new B series, is not as one would expect. The change in resistance of the higher nickel content compositions is $\approx 3\%$, and it is negative. This increase in resistance experienced by both the new and original D series is not expected from literature and requires further investigation. The effect of long term room temperature aging on the D series can at least be concluded to result in a decreased absolute change of resistivity, albeit a negative one.

The final puzzling result is the aging of the slow cooled E series. At most nickel contents, there appears to be almost no aging, except at Ni(x) = 0.6 and 0.65, where the change in resistivity becomes large, and negative. Perhaps these two outlying, negatively aged compositions were incorrectly sintered. To find whether some interruption during cooling might be the cause of these irregular results, new samples have been sintered at these compositions, but not yet tested.

The aging of the slow cooled series can also be compared to the results reported in Dr. Fritsch's doctoral thesis [52] (Figure 4.2). Unlike the correlation of results found for the B series, in this case the results are wildly different. The outliers at 0.60 and 0.65 nickel contents are already suspect, and unfortunately the referenced aging study did not include compositions with low nickel contents in the study. Perhaps these differences in aging behavior will decrease if the samples are allowed to age for a longer period of time.

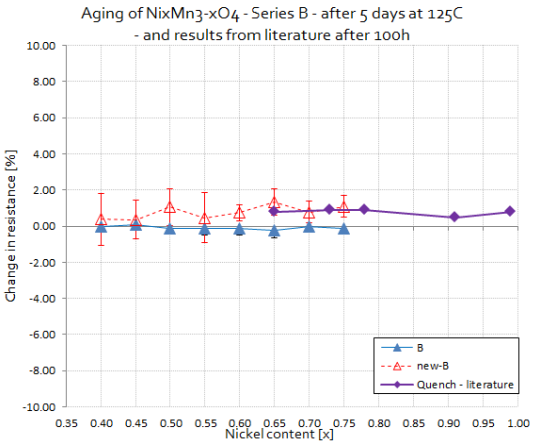

Figure 4.1: Resistance drift after 5 days at 125°C of quenched series B and new-B, as a function of nickel content for NTC samples of $Ni_xMn_{3-x}O_4$ composition as well as quenched series from Dr. Fritsch's doctoral thesis [52], aged for 100h.

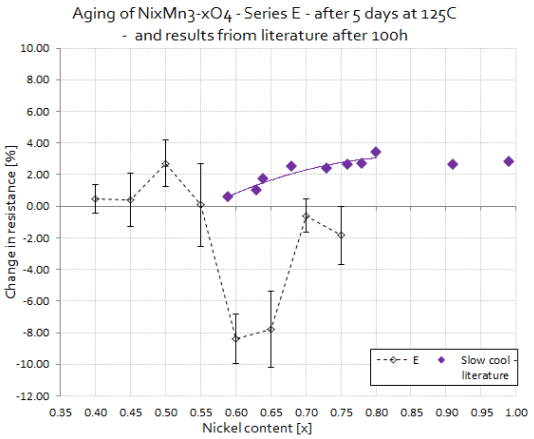

Figure 4.2: Resistance drift after 5 days at 125°C of slow cooled series E as a function of nickel content for NTC samples of $Ni_xMn_{3-x}O_4$ composition as well as slow cooled series from Dr. Fritsch's doctoral thesis [52], aged for 100h.

4.2 Phase formation

The composite scanning electron microscope (SEM) micrograph of the nickel manganite NTC's clearly shows that these ceramics can crystallize as a single phase spinel or segregate into a spinel and Ni-rich or Mn-rich phase, depending on the composition and cooling scheme. While the Ni-rich phase is commonly recognized as NiO, the exact composition of the Mn-rich second phase is unclear. The Wickham phase diagram (Figure 1.2), the most comprehensive phase diagram on nickel manganites to date, would lead one to the conclusion that the Mn-rich phase should be α-Mn_2O_3.

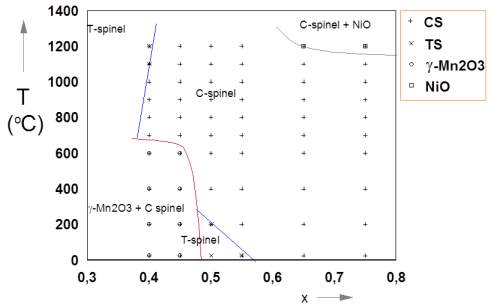

Figure 4.3: Phase diagram of $Ni_xMn_{3-x}O_4$ as determined by in-situ high temperature XRD in 2000.

In more recent publications [35, 53], the Mn-rich phase is identified as Mn_3O_4 from x-ray diffraction (XRD) analysis. However, thermal gravimetric analysis (TGA) analysis performed on these samples in 2000, in combination with in-situ high temperature XRD (Figure 4.3), indicate that the Mn-rich phase should be γ-Mn_2O_3.

The reason for the discrepancy in results is likely to stem from the fact that Mn_3O_4 is indistinguishable from γ-Mn_2O_3 using XRD, since their patterns overlap. Only TGA or Raman spectroscopy are able to differentiate between the two. [54]

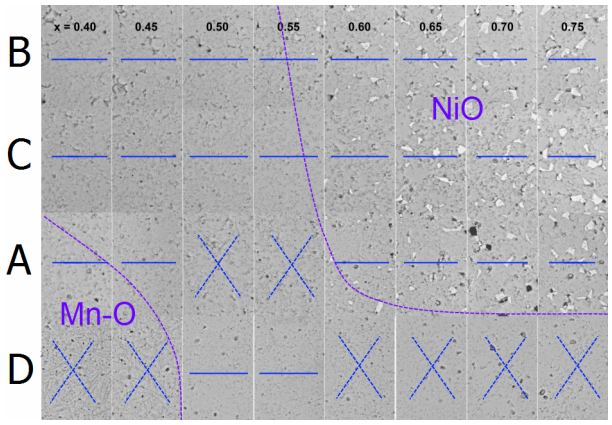

Figure 4.4: SEM micrographs of the cross-section of the pellets of series A-D for all compositions $0.4 < x < 0.75$, $Ni_xMn_{3-x}O_4$ taken in 2012 in BEC mode at 500x magnification. Crosses indicate compositions that do show detectable aging over 0.5% and lines indicate compositions that do not show detectable aging after the 33 day exposure to 125°C.

There may be some stability advantage for NTC compositions containing a NiO second phase. If the results of the 33 day aging study are superimposed onto the composite SEM micrograph (see

Figure 4.4, in which compositions that have detectable aging over 0.5% are indicated by a cross, and compositions that do not have detectable aging are indicated by a line), it becomes clear that all the compositions that contain NiO do not show detectable aging. The beneficial effect of NiO as a second phase is supported by the findings of Shpotyuk *et al.* [46, 48], Metz *et al.* [22], and Vakiv *et al.* [47].

There are only four other compositions that have not aged, and three of those appear to have a combination of a cubic and tetragonal spinel structure (evident from Figure 4.3):

- p530A: a cubic spinel with a Mn-rich second phase,
- p531A: a cubic/tetragonal spinel,
- p532D: a cubic/tetragonal spinel, and
- p533D: a cubic/tetragonal spinel.

The increased stability provided by NiO in the long term room temperature aged series is not reflected in the newly sintered series (new-A and new-B), however the phase formation of these compositions has not yet been verified with SEM.

4.3 Conclusions

This investigation confirms that the cooling conditions have a significant effect on the ultimate properties of the NTC. The aging characteristics and electrical properties of NTC samples with identical initial composition are vastly different, with the sole distinct variable being the cooling conditions.

The SEM investigation of the microstructure of the original A-D series confirms the original XRD analysis. Besides a nickel-manganite spinel phase, a second phase of nickel oxide is found for compositions with high nickel content. For all three of the A, B, and C series, as the Wickham phase diagram would lead one to expect. Yet for manganese rich compositions, the segregation of a manganese rich phase was identified in 530A, 530D and 531D, which is also expected.

During aging of all the NTC series, the quenched (B) and stoichiometrically cooled (C) series behave as expected. The original B and C series show no aging at all, even after 33 days, while the new-B series ages slightly, with a DR/R of $\approx +2\%$, which correlates to the results of Sophie Fritsch's doctoral thesis on Ni-Mn NTC's. The 3% decrease in resistance shown for the new-D series as well as the decrease reported for the slow cooled series E requires further study to fully understand.

Part II

Towards NTC Polymer Composites

CHAPTER 5

INTRODUCTION

Electroceramics, such as negative temperature coefficient of resistance (NTC) ceramics, offer a wide range of functional properties, from the temperature sensors described in Part I to ultrasonic transducers and high sensitivity actuators. Unfortunately, electroceramics are also stiff, brittle and heavy, none of which are qualities desirable in aerospace industries. To overcome the mechanical issues inherent to ceramics, the flexibility of polymers can be combined with the functionality of electroceramics, in the form of functional granular composites (FGC).

A flexible temperature sensor, which retains decent mechanical performance and formability while maintaining the sensitivity, response time and cost of NTC ceramics would be an interesting alternative for aerospace applications. The objective of the coming chapters is to investigate the prospects and pitfalls of producing an electrically conductive NTC polymer composite.

5.1 Functional granular composites

To distinguish between different types of FGC, Newnham *et al.* [55] devised a set of universal terminological conventions (shown in Figure 5.1). They divided the FGC by the degree of connectivity between the phases in a binary composite, where the first digit represents the connectivity of the filler (or ceramic), and the second the connectivity of the matrix (or polymer). 0-3 composites experience only minor connectivity of the ceramic phase and exhibit relatively low functional properties as a result. 1-3 composites, on the other hand, with ceramic connectivity in at least one dimension, exhibit much higher functional properties due to the easy electrical and thermal conduction paths created by the columns. The functional properties of FGC's increase with increased connectivity of the ceramic phase, up until 3-3 composites which enjoy complete 3-D connectivity.

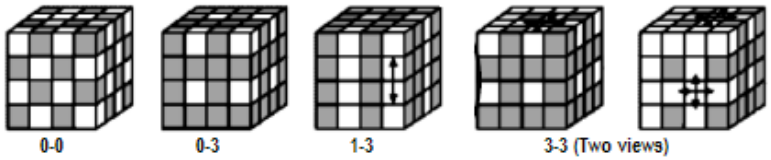

Figure 5.1: Illustration of the terminological conventions of diphasic composite-particulate connectivity. Arrows are used to indicate the connected directions (Adapted from Newnham *et al.* [55]).

In practice, 0-3 and 1-3 composites are preferred over 3-3 composites for their ease of manufacturing. The simplest kind of FGC to manufacture, 0-3 composites, are made by dispersing granules or particles of functional material randomly throughout a polymer matrix. In 0-3 conductive composites there is a certain minimum amount of critical volume of functional ceramic filler that must be added before the functional property becomes apparent. This limit is known as the percolation limit, and it represents the lowest volume fraction of functional filler that retains enough connectivity for the creation of conducting paths over the thickness of the composite. However, the increase in ceramic volume fraction also decreases the mechanical properties and increases cost.

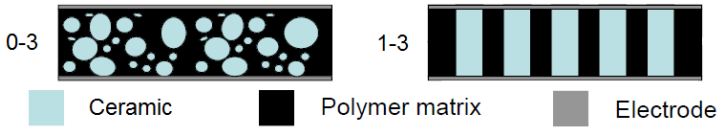

Figure 5.2: Illustration of the particle distribution in 0-3 and 1-3 ceramic-polymer composites

One solution to the decrease in mechanical properties is to induce increased connectivity between the particles by producing 1-3 composites instead. Structured 1-3 composites commonly consist of continuous fibers or oriented chains of ceramic particles, aligned in one specific direction (see Figure 5.2), which often necessitates complex fabrication methods. [56] The increased connectivity in 1-3 composites generally means that at much lower volume fractions of functional material, the composite will still show strong electromechanical properties. This lower volume fraction of brittle, ceramic particles, translates to an increase in the mechanical properties of the 1-3 composites and a decrease in cost. [57]

Due to the significant improvement of 1-3 composites over 0-3 composites, there is a great deal of interest in manufacturing them. Naturally, their fabrication is more complex, and several methods have been developed and used in industry today, such as: rod placement, dice and fill, lost mold method, injection molding, relic method, shaping of green ceramic mixture and structuring via dielectrophoresis (DEP). Most of these methods require complex shaping and each process has its own (dis)advantages when considering design freedom and cost.

In this light, dielectrophoresis has proven to be a relatively cheap and simple fabrication method, which offers a great deal of freedom in material tailoring for low volume fractions of electroceramic particles. [58]

This thesis will present an investigation into the prospects of producing an FGC temperature sensor, combining both the beneficial temperature sensing properties of NTC ceramics and the flexibility and ease of manufacturing available through polymer composites.

In the next section, a literature review will be presented on functional granular conductive composites. This is followed by a treatment of the results of the production of both 0-3 and 1-3 NTC composites in chapter 6. A discussion of the results gathered from the investigation into developing NTC composites will be presented in chapter 7. Finally, the conclusions of this study into NTC polymer composites will be provided along with recommendations for further work.

5.2 Literature review

NTC composites will potentially combine the considerable temperature sensitivity of thermistors with the mechanical flexibility and processibility inherent to polymers. In this study, NTC compos-

ites were developed and their temperature sensitivity and conductivity were measured. The interparticle distance of the NTC filler was investigated via scanning electron microscope (SEM), while the conductivity mechanism was evaluated through impedance spectroscopy.

Composite conductors, made by embedding conducting filler particles into an insulating, flexible, polymer matrix, find uses in any number of electronic applications, such as: temperature, infrared, chemical and magnetic field sensors, electromagnetic shielding, and solderless connectors.

To transform these composites from insulators into conductors, a characteristic amount of conductive filler must been added: the critical volume for percolation, ϕ_c, or percolation limit (Figure 5.3). At low volume percentages of conductive filler, the polymer matrix determines the composite properties. The composite will behave as an insulator, and take on the inherent resistivity of the matrix. Further addition of conductive filler allows the first continuous conduction paths to be formed within the composite. After which, mere incremental increases of the conductive filler induce a sudden switch from matrix-driven behavior to filler-driven behavior, transforming the composite into a conductor. Once this percolation limit (ϕ_c) has been reached, the electrical conductivity of the composite becomes comparable to its conductive constituent. [59]

The theoretical value of the percolation limit, when conducting particles are modeled as hard spheres packed at random on a regular lattice, corresponds to a volume fraction of 16%. In practice, the percolation limit of a certain filler/matrix can take on any value between 1 and 60vol%. [60]

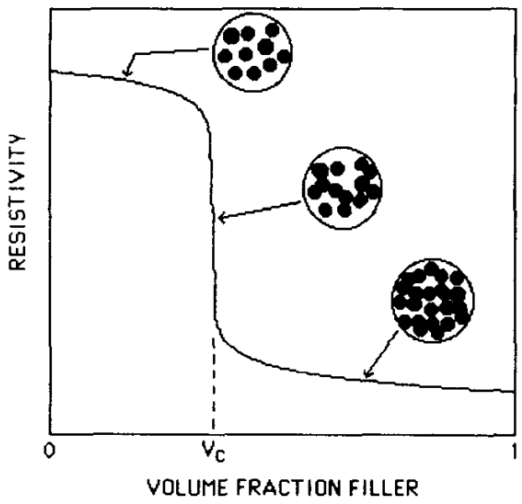

Figure 5.3: Percolation theory as applied to conductive composites. The formation of the first complete particle linkage results in a sharp drop in resistivity at ϕ_{crit}. [61]

The functional properties of conductive composites are not solely determined by the conductive constituent. The contribution of the polymer matrix to each conductive composite can tailor the resulting functional property. For example, heating a conductive filler-insulating polymer composite will lead to a positive temperature coefficient of resistance (PTC) effect as the conductive particles are pulled further apart at higher temperatures. Careful selection of the functional and mechanical properties of each composite constituent can lead to product properties such as: magnetoelectricity, pyroelectricity and photostriction. [59]

This section will introduce many concepts which factor into the electrical conductivity of conductive composites. Starting, with a treatment of the various contributions that directly effect the electrical

resistance of conductive composites in subsection 5.2.1. The geometrical effects of both the particles and sample dimensions will be discussed in subsection 5.2.2. The effects of temperature and pressure on conductive composites will then be discussed in subsection 5.2.3. Finally, a review of the existing models for conductive composites will be given in subsection 5.2.4.

5.2.1 Resistance in composites

In conductive composites, the resistance depends on the inherent properties of the conductive filler, but also the resistance due to the transference of electricity from one particle to the next. Yasuda and Nagata devised a general relation of the resistance in conductive composites, given by:

$$R_c = 2R_e + \frac{(M-1)R_p + MR_i}{N} \tag{5.2.1}$$

Where:

- R_c is the composite resistance,
- R_e is the lead resistance to electrodes,
- R_p is the particle-particle contact resistance,
- R_i is the resistance across one particle,
- M is the number of particles forming one conduction path, and
- N is the number of conduction paths.

In this relation, it is assumed that the filler volume content is over the percolation limit, and the maximum number of particles within the composite are contributing to the electrical conductivity. The lead resistance to electrodes, R_e, can be eliminated if a four-point-probe resistance measurement is used, simplifying the equation. The resistance across one particle, R_i, is an inherent property of the filler and so can not be changed, unless the filler is altered. In order to quantify the number of conduction paths, N, and the number of particles in each, M, conduction paths within conductive composites are assumed to be straight and parallel in arrangement, akin to a simple cubic packing. The number of conduction paths, N, can then be determined by geometrical constraints:

$$N = \frac{wt}{d^2} \tag{5.2.2}$$

Where:

- d is the particle diameter, and subsequently d^2 is the cross-sectional area of one chain and its surrounding insulation (For the purposes of this discussion, the conductive filler particles are assumed to be spherical),
- w is the width of the composite, and
- t is the thickness of the composite.

While the number of particles contained in each chain follows from:

$$M = \frac{L}{d} \tag{5.2.3}$$

Where L is the length of the composite.

Even though the assumption of cubic packing is clearly ludicrous for actual composites, these simplifications make one point abundantly clear: besides geometrical factors, it is the particle-particle contact resistance R_p, which represents the most important constraint on composite conductivity.

In general, the main restrictive factors to particle-particle resistance can be subdivided into three main contributors: constriction resistance, tunneling resistance and deformation dependent resistance.

Constriction resistance

In any medium, when two conductive spheres come into contact with one another, there is a resistance which results from an incomplete transfer of electricity. This constriction of conductivity is shown graphically in Figure 5.4, where each entire spherical particle is capable of conductivity over its entire diameter, D, however the flow of electricity from one sphere to the next is constricted to the much smaller diameter, d, of the contact between the spheres. This constriction resistance (R_{cr}), due to decreased available diameter for conductivity, is characterized by: [61]

$$R_{cr} = \frac{\rho_i}{d} \tag{5.2.4}$$

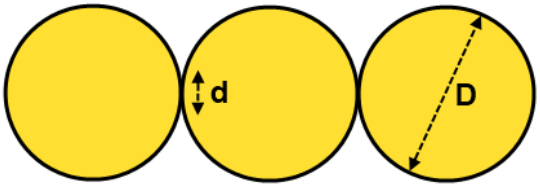

Figure 5.4: Conductive spherical filler of particle size D showing the contact diameter d through which conduction must take place within an insulating matrix.

Where:

- ρ_i is the intrinsic resistivity of the filler, and
- d is the diameter of the contact spot.

If ratio of particle size to contact diameter is large, even though the particles may still be in physical contact, the constriction resistance becomes so high that almost all conductivity is lost. The upper limit of particle size to contact diameter (D/d) is around 10. [61]

Tunneling resistance

Within a conductive composite, it is probable that not all particles will be in perfect contact with one another, but that instead, there is some insulating film around each particle which must be overcome for conductivity to take place. An example of such a film is shown in Figure 5.5 and represents the second important contributor to resistance between conductive particles in a medium.

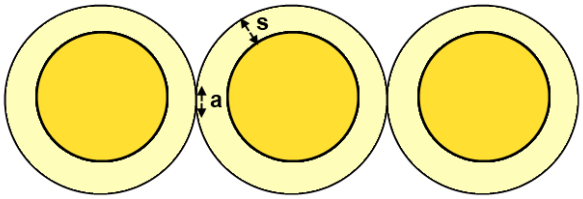

Figure 5.5: Conductive spherical filler with an insulating film of thickness s around each particle, showing the contact area a through which conduction must take place within an insulating matrix.

While preparing conductive filler particles, the powder can be exposed to air (creating a thin oxide layer over each particle), or a binder can be added to increase flowability. Three separate types of films are identified as the cause of decreased conductivity in conductive composites: (1) oxide layers, (2) residual organic films (or binder) added for powder processing, and (3) the polymer matrix itself. If the total thickness of these three layers (a) becomes too large all conductivity is negated, however for thin films on the order of 100 quantum-mechanical tunneling can occur. This form of resistance is termed tunneling resistance (R_t), and is characterized by: [61]

$$R_t = \frac{\rho_t}{a} \tag{5.2.5}$$

Where:

- ρ_t is the tunneling resistivity which can be applied to the contact if the film thickness s is known, and
- a is the area of the contact spot.

Since the film layer must be relatively thin in order for the electron tunneling to take place, the contribution of R_t to the total resistance is minor. [60] Surprisingly, the resistivity of the medium (or polymer matrix) does not contribute to the tunneling resistance. The probability of electron tunneling only depends on the properties of the conductor, the thickness of the film (a) and the relative dielectric permittivity of the film. [61]

The total resistance of the contact between spherical conductive particles in a medium (R_c) is the sum of both the constriction and tunneling resistance, and is equal to:

$$R_c = \frac{\rho_i}{d} + \frac{\rho_t}{a} \tag{5.2.6}$$

Deformation dependent resistance

The third contributor to resistance between touching conductive particles is derived from the size of the contact spot between them. The diameter of the contact spot between spherical particles is calculated from:

$$d = (\frac{4a}{\pi})^{\frac{1}{2}} \tag{5.2.7}$$

However, the diameter of the contact spot is not only a geometrical property, it also depends on the applied pressure between the particles, F. When two spheres experience an applied stress, the contact diameter between them increases, and when the contact diameter increases, this has a direct effect on the constriction resistance, see (5.2.4).

Wagar [62] shows that for electrical contacts, the strains needed to reduce the constriction resistance (ie: to reduce the particle size to contact size ratio, D/d, below the aforementioned critical value of 10), are larger than the elastic yield strain. So, for electrical contact, both elastic and plastic deformation must occur. The two contributing factors to deformation of the contact area are calculated from: [61]

$$a_{plastic} = \frac{F}{H} \tag{5.2.8}$$

$$a_{elastic} = 2.43(\frac{FD}{E})^{\frac{2}{3}} \tag{5.2.9}$$

Where:

- H is the contact hardness, and
- F is the applied pressure between particles.
- D is the sphere diameter, and
- E is the elastic modulus.

Since, most deformations are a combination of plastic and elastic deformation, a simplified version of the contact area calculation for both effects is given by: [61]

$$a = \frac{F}{\xi H} \tag{5.2.10}$$

Where:

- ξ ranges from 0.2 for purely elastic deformation to 1.0 for purely plastic deformation (a value of 0.7 has been found to be reliable for most systems) [61].

Filling in these new relations for the contact area into the previous summation of the constriction and tunneling resistance (5.2.10), leads to a new formula for the particle-particle resistance in terms of known material parameters and the applied force:

$$R_{p-plastic} = 0.89\rho_i(\frac{\xi H}{F})^{\frac{1}{2}} + \rho_t\frac{\xi H}{F} \tag{5.2.11}$$

$$R_{p-elastic} = 0.57\rho_i(\frac{E}{FD})^{\frac{1}{3}} + 0.26\rho_t(\frac{E}{FD})^{\frac{2}{3}} \tag{5.2.12}$$

These first models of the resistance in conductive composites give a reasonable indication of the variables that determine the resistivity of a conductive composite. The next section will focus more clearly on the direct geometrical effects.

5.2.2 Geometry effects on percolation

As long as the conductive filler volume content in a conductive composite remains below the percolation limit, the composite will behave as an insulator. The value of the percolation limit, ϕ_c, is characteristic for a certain match of filler and matrix, but it can be adjusted through changes in particle size or sample size and shape. Two characteristic ratios which determine the critical volume content for percolation are distinguished. The first is the geometry factor, G, given by: [59]

$$G = \frac{A}{t} \tag{5.2.13}$$

Where:

- A is the area of the electrode, and
- t is the thickness of the sample, or distance between the electrodes.

The second characteristic ratio which affects the percolation limit is the ratio of the particle size to the smallest sample dimension, Γ, which is calculated from:

$$\Gamma = \frac{t}{d} \tag{5.2.14}$$

Where:

- t is the smallest sample dimension, which for the purposes of this discussion will always be the thickness of the sample, and
- d is the particle size of the filler.

Adjusting either G or Γ results in a change in the percolation limit of the conductive composite. For example, at constant particle size, increasing Γ (so decreasing the sample thickness) will increase the percolation limit (Figure 5.6). This effect becomes far less pronounced the smaller the particle size becomes, as shown in Figure 5.7. [63]

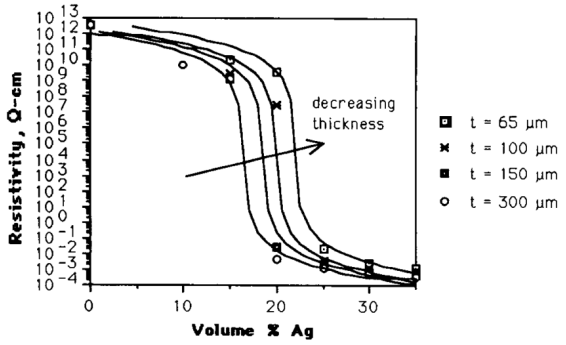

Figure 5.6: Percolation curves for 9.0μm Ag powder filled silicone rubber composites, for decreasing sample thickness (with mathematical curve fits). [63]

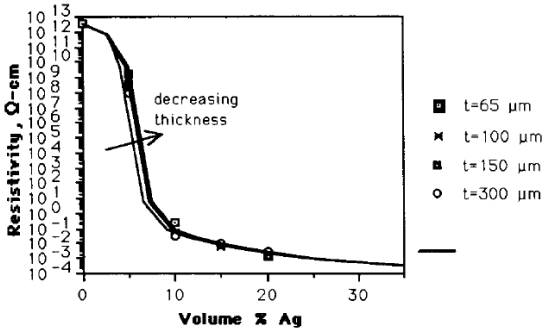

Figure 5.7: Percolation curves for 0.5μm Ag powder filled silicone rubber composites, for decreasing sample thickness (with mathematical curve fits). [63]

The reason for the decreased effect of sample dimensions at smaller particle size is due to the differences in the particle size of the filler and matrix particles. The smaller the filler particles become, relative to the matrix particles, the easier it becomes for the filler to form continuous conduction paths (illustrated in Figure 5.8). When the conducting particles are small, they are forced into interstitial sites between the insulating particles. At these interstitial sites, the conductive filler particles enjoy a greater degree of contact, which results in a lower required volume content for percolation within the composite. Consequently, if the conducting particles become too large to fit into the interstitial sites, the distances between each particle become much larger, and a greater volume fraction is required for conductivity (Figure 5.8(a)). [59]

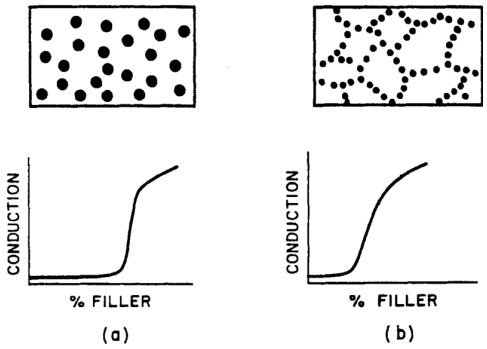

Figure 5.8: Mixing of filler particles of equal size to the matrix (a), and filler particles of a smaller size than the matrix (b). The percolation limit decreases when the filler particle size is small enough to fit into interstitial sites between the insulating matrix particles. [59]

The direct effect of both G and Γ can clearly be shown through a qualitative representation of the percolation behavior as a function of resistivity, volume fraction of filler and either G or the particle size (Figure 5.9). Increasing either G or Γ will decrease the amount of conductive filler required for percolation, while decreasing either will serve to increase the amount of conductive filler required.

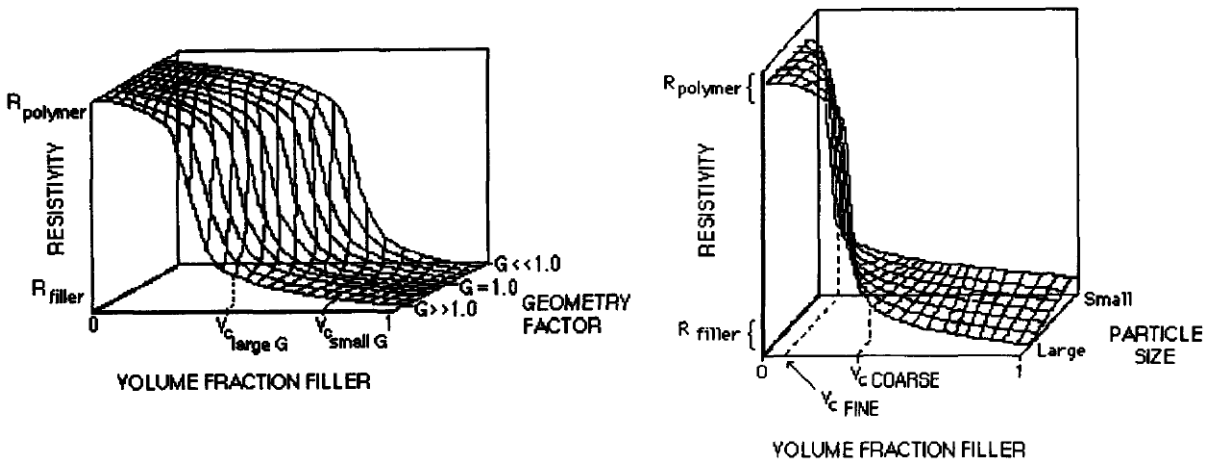

Figure 5.9: Qualitative representation of the percolation behavior of composites as a function of the geometry factor G (left) and the particle size to sample thickness ratio Γ (right). [63]

The geometrical parameters of both the conductive filler and the composite sample are of great importance when designing any conductive composite. The lower the percolation limit of the composite,

the less conductive filler is required for conductivity which directly translates to a decrease in cost as well as an increase in mechanical flexibility.

5.2.3 Temperature and pressure effects

The conductivity of electrically conductive composites is also influenced by changes in temperature and pressure. The effect of the application of stress on conductive composites was already briefly presented in the previous discussion on constriction resistance (see subsection 5.2.1). Pressure induced changes in resistance are most prominent at volume fractions close to the percolation limit of the conductive composite, shown in Figure 5.10 at both increased uniaxial pressure (left) as well as increased hydrostatic pressure (right). Persistent changes in resistance, due to applied pressure, are mainly due to creep of the polymer matrix. [64]

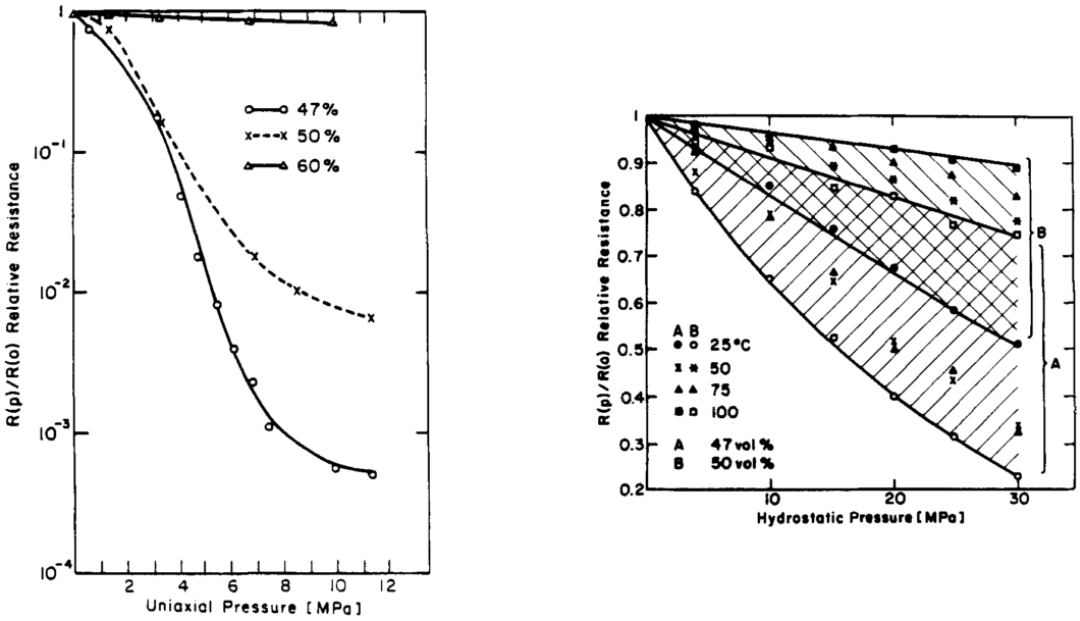

Figure 5.10: Relative change of dc resistance of Fe_3O_4-epoxy composites at varying volume percentages of conductive filler as a function of uniaxial pressure (left) and hydrostatic pressure as well as temperature (right). [64]

Electrically conductive composites can show both NTC and PTC behavior. One such example is a V_2O_3-polyethylene composite, shown in Figure 5.11. Before percolation, the composite behaves as an insulator. Once the percolation limit (at approximately 30vol% V_2O_3) is breached, the semiconductor-to-metal transition at -120°C of the filler becomes apparent. The resistivity drops, and remains low until the composite approaches the melting temperature of the semicrystalline polymer at +120°C at which point the resistivity rises once again. This PTC effect is ascribed to the expansion of the polymer at its own transition temperature, separating the conductive particles from one another. [60]

The severity and nature of the effect of temperature and pressure depends greatly on the type of filler and matrix chosen for the conductive composite. Each match would have to be tested to discover the specific response of the particular resulting conductive composite.

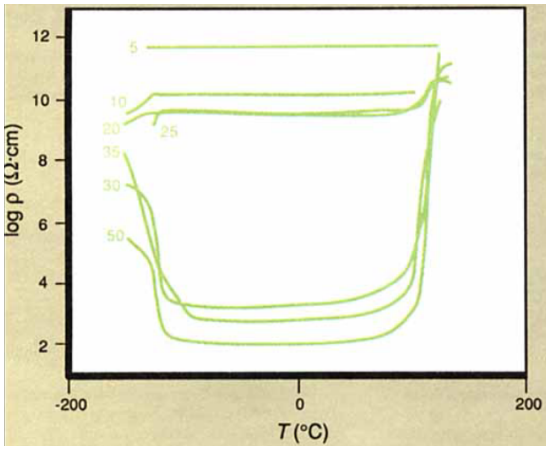

Figure 5.11: Resistivity versus temperature of V_2O_3-polyethylene composites at varying volume percentages of conductive filler. [60]

5.2.4 Modeling conductive composites

The most simple models applied to predict the conductivity of binary composites are the parallel and series addition models. These two addition approximations assume that the binary composite consists of perfectly separate slabs of both conductive filler and insulating matrix, either stacked in series or parallel to one another, with respect to the current (see Figure 5.12). The series addition approximation represents the minimum conductivity one could expect from any binary composite at each volume fraction of conductive filler, while parallel addition represents the maximum. Series addition follows from:

$$\rho_m = \phi\rho_l + (1-\phi)\rho_h \tag{5.2.15}$$

Where:

- ϕ is the volume content of filler in the composite,
- ρ_h is the resistivity of the insulating polymer matrix,
- ρ_l is the resistivity of the conductive filler, and
- ρ_m is the resistivity of the composite.

While parallel addition is calculated from:

$$\frac{1}{\rho_m} = \frac{\phi}{\rho_l} + \frac{(1-\phi)}{\rho_h} \tag{5.2.16}$$

A more general approach to calculating these bounds, is found through the rule of logarithmic mixing, or Lichtenecker's rule. Lichtenecker's rule bridges the gap between a perfect series and perfectly parallel structure within a composite, and is modeled by varying the factor n, from -1 (or, parallel addition) to +1 (or, series addition):

$$\rho_m^n = \phi\rho_l^n + (1-\phi)\rho_h^n \tag{5.2.17}$$

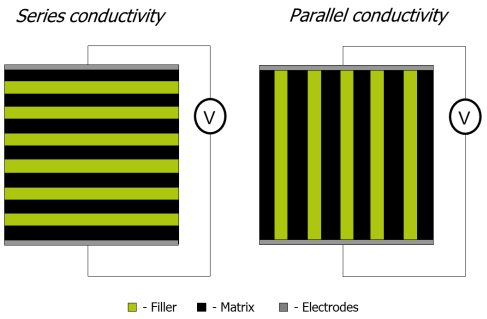

Figure 5.12: Visualization of idealized series and parallel connectivity.

The Lichtenecker model can be used to gauge what sort of connectivity is dominant within a binary composite. It does not take percolation into account, at which point the conductivity switches from series driven behavior to parallel driven.

To more accurately model the percolation induced switching in isotropic binary conductive composites as a function of volume content, the Bruggeman general effective media (GEM) equation is applied. The GEM equation continuously interpolates between the two classical percolation equations, generating a quantitative fit for experimental data. The GEM equation is an implicit function, given by: [60]

$$\frac{(1-\phi)(\rho_m^{\frac{1}{t}} - \rho_h^{\frac{1}{t}})}{\rho_m^{\frac{1}{t}} + A\rho_h^{\frac{1}{t}}} + \frac{\phi(\rho_m^{\frac{1}{t}} - \rho_l^{\frac{1}{t}})}{\rho_m^{\frac{1}{t}} + A\rho_l^{\frac{1}{t}}} = 0 \tag{5.2.18}$$

Where:

- t is an empirically found exponential factor for each filler/matrix combination, and
- A is a constant in the Bruggeman-GEM equation which depends on the critical volume content ϕ_c given by: $A = \frac{1-\phi_c}{\phi_c}$.

The conducting particle shape and spatial distribution, as well as their interconnectivity is taken into account by the GEM equation, and characterized by the exponent t and the critical volume fraction ϕ_c.

CHAPTER 6

RESULTS

The resistivity and characteristic B-value of negative temperature coefficient of resistance (NTC) thermistor composites are a function of the NTC volume fraction ϕ, the calcined NTC powder properties and the interparticle distance between individual NTC particles. The experimental method applied in manufacturing and measurement of all NTC polymer composites is described in section 6.1. The results of varying the NTC filler volume content in 0-3, 1-3 and agglomerated NTC polymer composites are presented.

6.1 General experimental methodology

All NTC composites were prepared according to the general experimental method laid out in the following sections. Most composites produced are 0-3 (randomly oriented) conductive NTC filler - insulating epoxy matrix composites. The dielectrophoretic processing applied to produce structured NTC composites is also laid out. The specific materials and equipment employed in the composite production and analysis will also be detailed.

6.1.1 Composite manufacturing

All NTC composites were manufactured with a mixture of an epoxy system and NTC nickel-manganite spinel powder. The NTC powder used in this study was a powder which is used industrially for sintering NTC bulk ceramics (P64591, Vishay BC Components, Brussels, Belgium). The as received powder was calcined at 850,900 and 950°C for four hours (heated at 350 K/h) in a Nabertherm high temperature furnace, and allowed to cool to room temperature. A tetragonal spinel structure was achieved at the calcination temperature of 950°C, as verified by x-ray diffraction (XRD) with a D4 Endeavor diffractometer using Cu-Kα.

The agglomerated powder was milled for 16 hours to a micrometer range size distribution of 1μm to 10μm, with remaining agglomerates of size distribution 40μm to 250μm, by using a Gladstone Engineering Co. Ltd. roll bench. The attained particle size distribution was measured using a Beckman Coulter Laser Diffraction Particle Size Analyzer. The NTC powder was sieved through a 125μm sieve, and a 63μm sieve to remove agglomerates. The structure of the NTC powder was verified after milling by XRD with a Bruker D8 Advance diffractometer using Cu-Kα. The resistivity of the calcined powder is approximately $5{\cdot}10^5\Omega$.cm.

An epoxy system (Epotek 302-3M, Epoxy Technology Inc., Billerica, Ma, USA) which consists of two separate components, one a diglycidyl bisphenol-A (DGEBA) resin and the other a poly(oxypropyl)-diamine (POPD) multi-functional aliphatic amine curing agent, was chosen. This epoxy is recommended for adhesive joining, sealing, potting or as a coating. It has excellent water, chemical and solvent resistance properties, and is used in combination with semiconductors for underfilling. The glass transition temperature (T_g) of the epoxy is $\approx 55°C$. Its coefficient of thermal expansion (CTE) below T_g is $56 \cdot 10^{-6}$ in/in/°C, and above T_g it is equal to $193 \cdot 10^{-6}$ in/in/°C. The epoxy degrades at $\approx 350°C$, and can cure at any temperature between 20 to 200°C.

At room temperature the epoxy is viscous (at 800 - 1600 cPs) and has a dielectric constant (at 1 kHz) of approximately 3.4, which makes it an interesting option for attempting dielectrophoresis (DEP). The volume resistivity of the epoxy is on the order of 10^{14} Ω.cm, which is a great deal higher than the NTC powder.

Each composite was fabricated by mixing the epoxy resin and ceramic particles together at high speed in a planetary mixer (SpeedMixer DAC 150.1 FVZ, Hauschild). First the NTC particles were dispersed in the resin only, by mixing at 1500 rpm for 15 minutes. Next, the hardener was added and the composite resin was mixed again, this time at 1500 rpm for 2 minutes. The composite resin was then poured into a mold (Figure 6.1). The mold consisted of a Teflon spacer of 1mm thickness with four equally spaced 15mm diameter circular cut-outs. Two layers of 50μm thick Al foil are placed on either side of the spacer, which act as the electrodes for the application of the electric field for DEP. This setup was bolted between two steel plates to apply pressure to the mold and produce flat samples. To avoid short circuits in 1-3 samples, additional 1mm Teflon layers were placed between the steel plates and the Al electrodes.

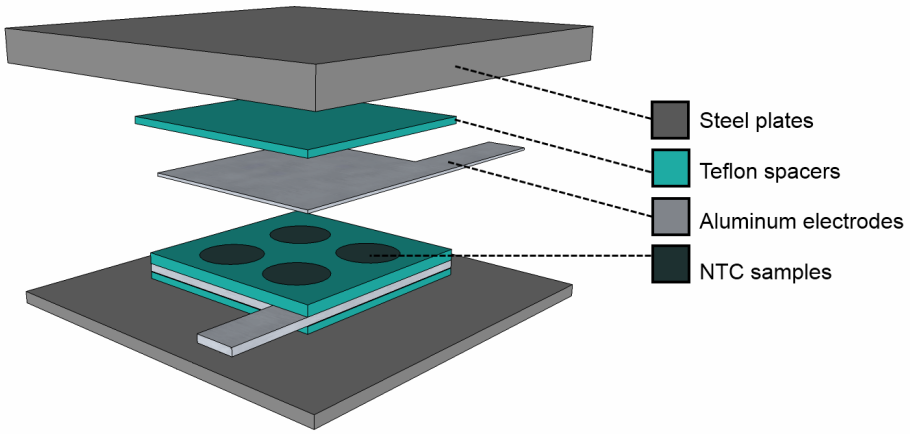

Figure 6.1: Schematic drawing of the mold used for processing the (dielectrophoretically structured) NTC composites.

In order to produce 1-3 samples, a dielectrophoretically structuring electric field was applied. A function generator (Agilent, 33210A) was coupled to a high voltage amplifier (Radiant Technologies Inc., T6000HVA-2) for application of the electric field (Figure 6.2). Next, the electric field was applied over the mold. The peak to peak output of the high voltage amplifier, the phase angle and the leakage current were verified with an oscilloscope (Agilent, DSO-x 2004A). The electric field was applied for a minimum of 3 hours, after which the mold was heated in situ at 50°C to allow the composite to cure. The dielectrophoresis was performed at room temperature. Samples of 1mm thickness with an

NTC volume fraction between 15 and 30vol% were processed at a fixed sinusoidal electric field with an amplitude and frequency tailored to each volume fraction of filler for optimum structuring.

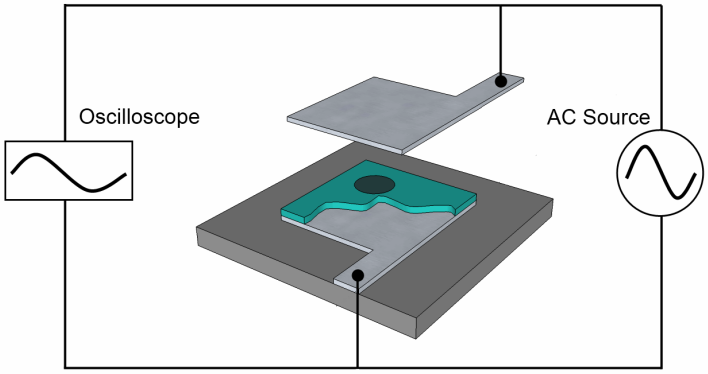

Figure 6.2: Visualization of connections for the AC source and oscilloscope in the DEP experimental set up.

Randomly oriented (0-3) samples of 1mm thickness with an NTC volume fraction between 15 and 50vol% were cured without applying an electric field and allowed to cure overnight in an oven at 50°C.

After curing, all samples were ejected from the molds and polished to remove the top layer of polymer on the composite and post cured for 1 hour at 100°C to remove moisture. Finally, electrodes were applied directly on the surface of the composite samples by sputtering 10mm diameter, 20nm thickness, circular gold electrodes on both sides (Balzers Union, SCD 040). Even though the electrodes were applied in a consistent manner the electrode adhesion on the NTC composite samples is not always reliable.

6.1.2 Measurement procedures

Ac resistance measurements were performed at 25°C and 85°C using an ac resistance meter (HP 4276A LCZ meter) set to a frequency of 1kHz and a voltage of 1000mV. Consistent measurement temperatures were ensured by dipping the samples in a water-cooled Julabo, SE Class III, 12876 oil bath.

Dc resistance measurements were performed at room temperature using an Agilent 4339B high resistance meter in combination with an Agilent 16339A component test fixture set to a voltage of 10V for high resistance, and a HP 3478A multimeter set to a dc bias of 1V for low resistances.

The microstructure of the samples was observed using a field emission - scanning electron microscope (FE-SEM) (JEOL, JSM-7500F) operated in backscattered electron (composition) mode. Samples sectioned parallel to the formed particle chains were embedded into a room temperature curing epoxy and polished with 1μm diamond paste. The SEM micrographs of sample cross sections were analyzed with MATLAB.

6.2 Varying volume fraction of 0-3 and 1-3 composites

The resistivity at room temperature of both 0-3 and 1-3 composites is shown in Figure 6.3. At low volume contents of conductive filler, the resistivity of the NTC composites is equal to that of the epoxy matrix, regardless of structurization. While the resistivity does decrease with increasing filler volume content, the resistivity of the composites does not approach that of the bulk ceramic.

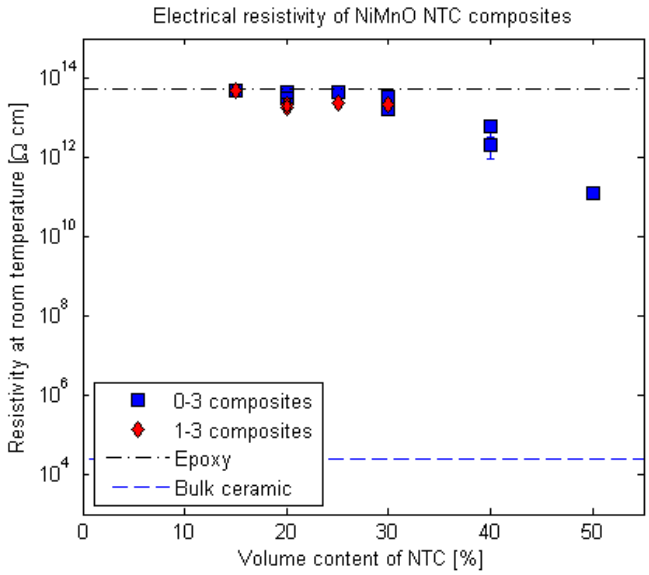

Figure 6.3: Resistivity at 25C of 0-3 and 1-3 NiMnO and Epotek epoxy composites.

Since the homogeneous 0-3 composites do not appear to achieve percolation, an experiment was carried out to examine the effect of inhomogeneous mixing on the conductivity in NTC polymer composites. Three types of mixing are distinguished in Figure 6.4: homogeneous (mixed in the speed mixer for 15 minutes), intermediate (hand mixed), and agglomerated (hand mixed using agglomerated powder, that was not sieved)).

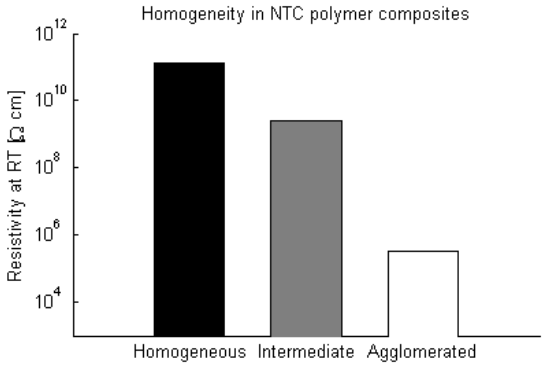

Figure 6.4: Resistivity at room temperature of 50vol% 0-3 composites with decreasing homogeneity.

The composite with the highest degree of inhomogeneity (the hand mixed, agglomerated composite) also has the highest conductivity. Similarly hand mixed composites were manufactured at volume fractions of 35% and 45%, and the results are shown in Figure 6.5.

The critical NTC volume content for percolation ϕ_c is presented in Figure 6.5, and modeled through the Bruggeman-general effective media (GEM) equation to be between 30 to 40vol% for this particluar combination of particle size and sample geometry. Before percolation the resistivity of the NTC composites is equal to that of the epoxy matrix, regardless of structurization. The resistivity of the NTC composite after percolation is in the range of 1 - 2 $\cdot 10^5 \Omega$.cm, still above the resistivity of the sintered bulk ceramic at $2.55 \cdot 10^4 \Omega$.cm.

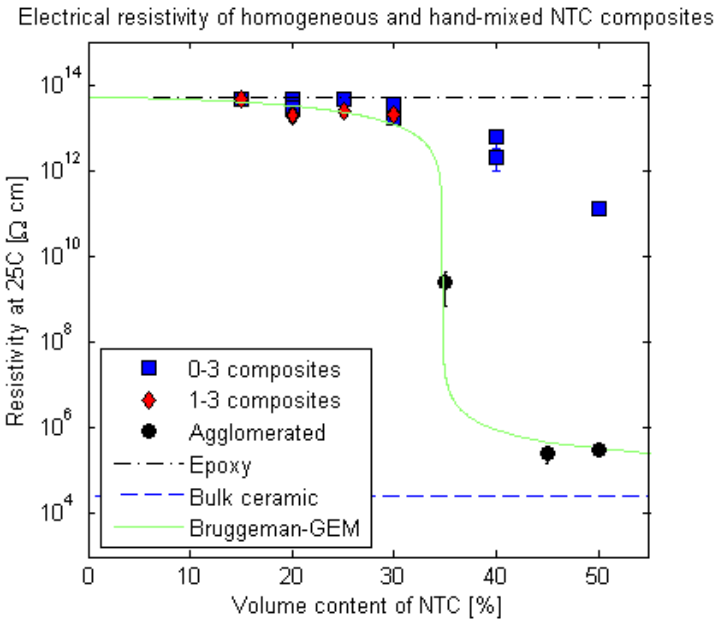

Figure 6.5: Resistivity at 25C of 0-3, 1-3 and agglomerated NiMnO and Epotek epoxy composites.

The B-value of the NTC composites is presented in Figure 6.6. Before percolation, the B-value of both random and structured NTC composites is within the range of the epoxy matrix. Immediately after percolation, the B-value jumps to a positive value in the range of 1500K, dependent on NTC filler volume content.

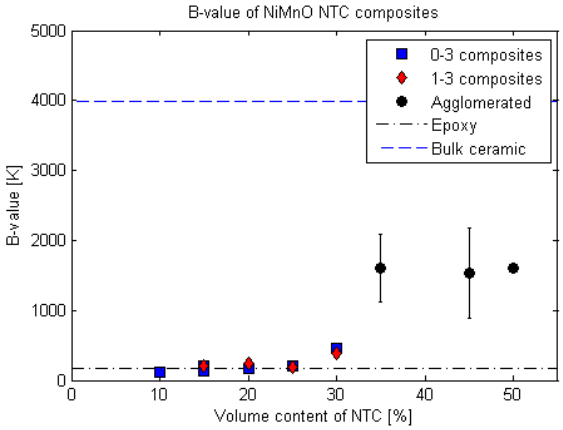

Figure 6.6: B-value of 0-3, 1-3 and agglomerated NiMnO and Epotek epoxy composites

Even though there appears to be no improvement in the electrical properties of the 1-3 composites over the 0-3 composites, the semiconducting NTC particles are still susceptible to the dielectrophoretic effect. To visualize the motion of NTC particles due to the DEP force, a droplet of an uncured homogeneously mixed 2vol% NTC polymer composite is placed on top of a glass plate between two silver electrodes (shown schematically in Figure 6.7).

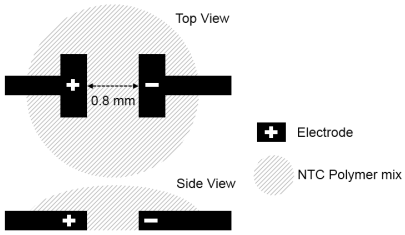

Figure 6.7: Schematic of DEP setup for in situ images. A droplet of a homogeneously mixed NTC composite (striped) is placed between two silver electrodes (black), on a glass plate (Top and side view).

A low voltage is applied, and the NTC particles immediately begin to move as a consequence (Figure 6.8). First the voltage is kept at a constant 1V, while the frequency is increased up to 2.5kHz at t = 30s, after which the voltage is increased up to 4V at t = 150s, at constant frequency. Alignment of the NTC particles between the electrodes can be seen most clearly at t = 30s, after which the space between the electrodes becomes far too dense to be able to distinguish one chain from another.

Interestingly enough, even at such low vol% there is enough NTC filler to produce a short circuit between the electrodes (Figure 6.9).

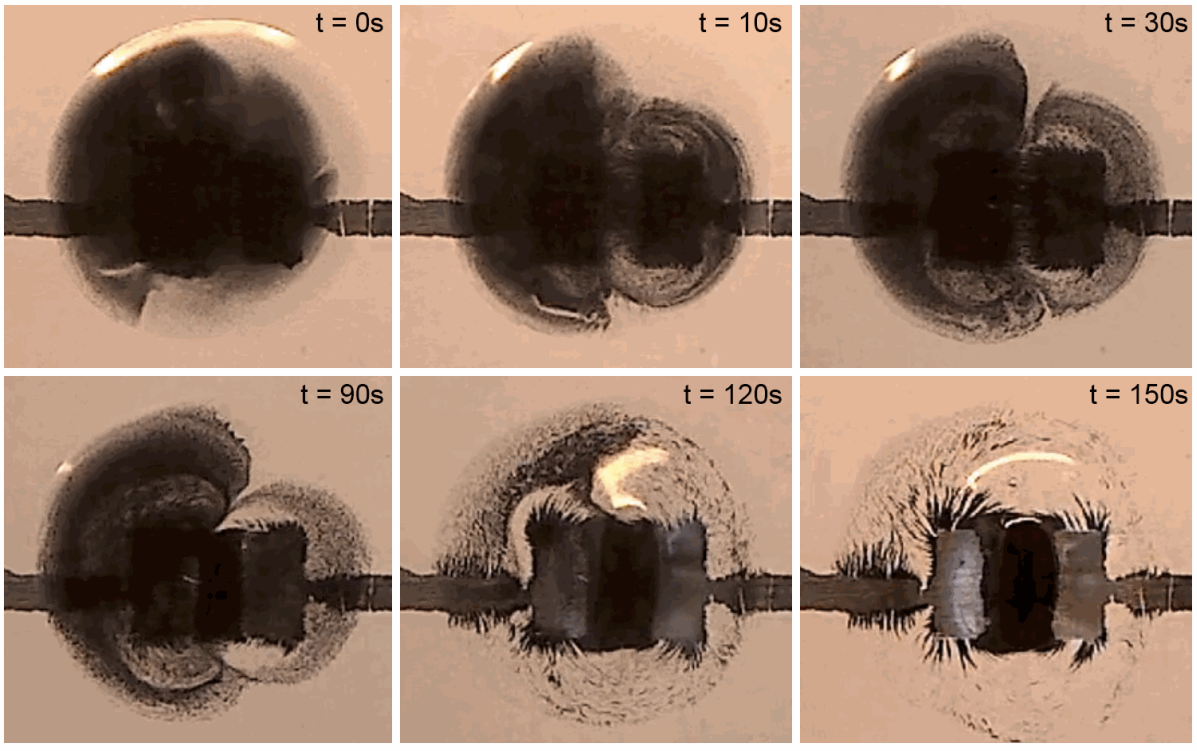

Figure 6.8: Motion of NTC particles in a liquid epoxy matrix as a function of time, due to DEP (Top view).

Figure 6.9: Short circuit during dielectrophoresis of NTC particles in a liquid epoxy matrix due to percolation of the NTC particles between the electrodes (Top view).

6.3 Duplicating series connectivity

In order to investigate the insulating effect of the Epotek epoxy used in all NTC polymer composites, a facsimile of series connectivity is produced by layering sintered NTC ceramics with Epotek epoxy (shown in Figure 6.10). Ten different NTC-epoxy stacks are manufactured with varying amounts of Epotek epoxy, by applying a droplet of epoxy onto the surface of the bottom NTC pellet, and allowing the stack to cure at 50°C overnight.

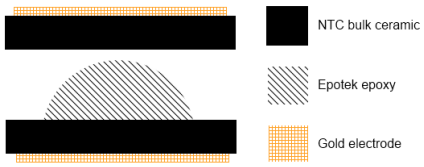

Figure 6.10: Schematic of the sintered NTC ceramic - epoxy stacks.

The resistivity of the cured NTC-epoxy stacks varies greatly depending on the thickness of the epoxy layer between them (Figure 6.11). Before processing, the resistivity of all the NTC pellets was $\approx 1.1 \cdot 10^3 \Omega$.cm. After adding an epoxy layer, the resistivity of the NTC-epoxy stacks ranges from $10^{12} \Omega$.cm, close to the resistivity of the epoxy, to $10^6 \Omega$.cm.

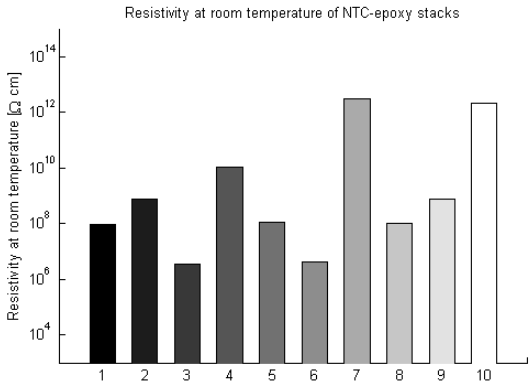

Figure 6.11: Resistivity of 10 different sintered NTC ceramic - epoxy stacks.

6.4 Increasing the pressure on 0-3 NTC composites

The application of uniaxial pressure to conductive composites is reported to decrease the resistivity of conductive composites (see subsection 5.2.3). To investigate whether this holds true for NTC composites, 0-3 50vol% NTC composites were subjected to increasing amounts of uniaxial pressure within a Simplimet II, Buehler Ltd. hot press (Figure 6.12). Each sample was heated to 130°C for 1 hour, after which a stress of 0, 4, 8, 16 and 32 MPa was applied. After cooling to room temperature, each sample was re-electroded through vacuum metalization with an electrode of 10mm diameter, while the diameter of the sample itself was punched back to its original size.

Figure 6.12: Simplimet II hot press.

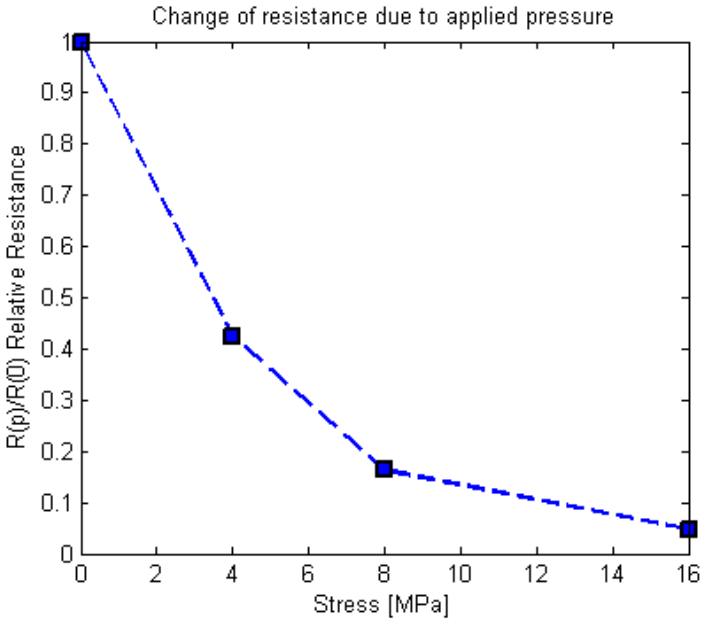

Figure 6.13: Pressure experiment on 50vol% NiMnO spinel NTC - Epotek epoxy composites

The relative resistance of the heated and stressed 0-3 50vol% NTC composites are presented in Figure 6.13. The resistance of all stressed NTC composites decreases after treatment. At 32MPa, the NTC composite becomes so thin and brittle as a consequence of the applied stress, that it breaks, and it is no longer possible to measure the resistance.

6.5 Interparticle distance of 0-3 and 1-3 NTC composites (SEM)

In order to determine the effect of the interparticle distance on the resistivity and B-value of NTC composites, 0-3 composites of 10 - 50vol%, 1-3 composites of 15 - 30vol% and stressed 0-3 composites of pressures equal to 16 and 32MPa were examined by SEM. Most NTC composite micrographs look similar to Figure 6.14 and 6.15, showing a homogeneous distribution of NTC particles within the epoxy matrix. However, at low volume fractions, the alignment of particles due to dielectrophoretic processing is clearly visible (Figure 6.16). The most striking result apparent from the SEM micrographs is that the hand mixed NTC composites with the lowest resistivities appear to contain a network of large agglomerations interspersed with less densely mixed regions (see Figure 6.17 and 6.18).

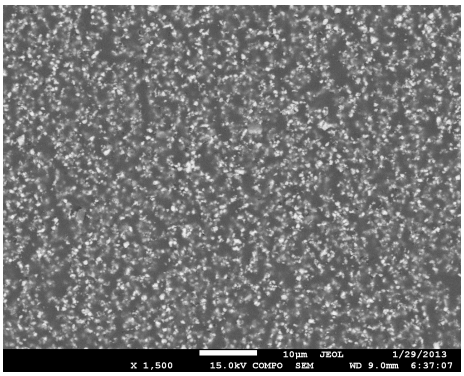

Figure 6.14: Example SEM micrograph of a homogeneous 0-3 15vol% NTC-epoxy composite at 1500x magnification.

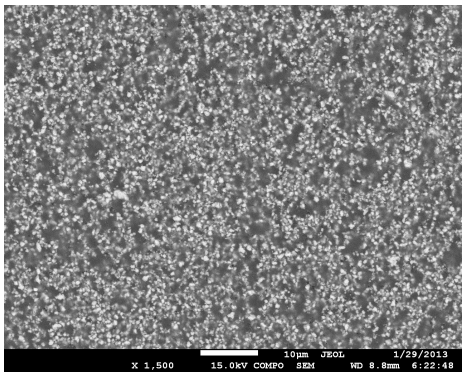

Figure 6.15: Example SEM micrograph of a homogeneous 1-3 25vol% NTC-epoxy composite at 1500x magnification.

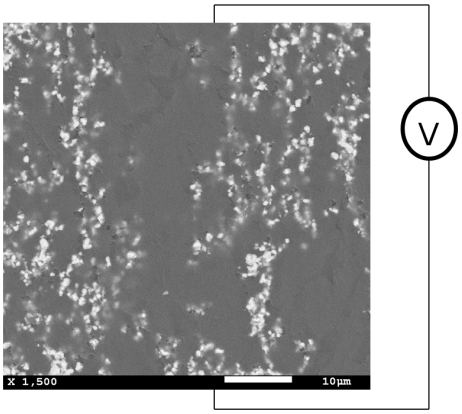

Figure 6.16: SEM micrograph of a 1-3 15vol% NTC-epoxy composite at 1500x magnification, showcasing the alignment of the NTC particles due to DEP, and the direction of the applied voltage.

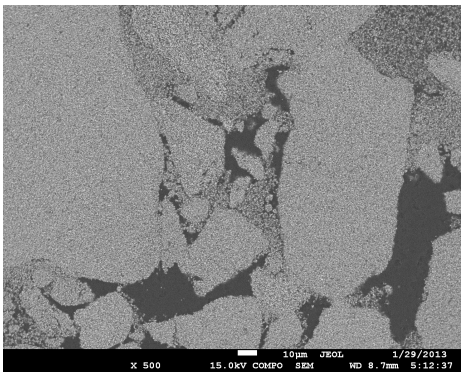

Figure 6.17: SEM micrograph of a 0-3 45vol% NTC-epoxy composite at 500x magnification, showcasing the agglomoration of particles.

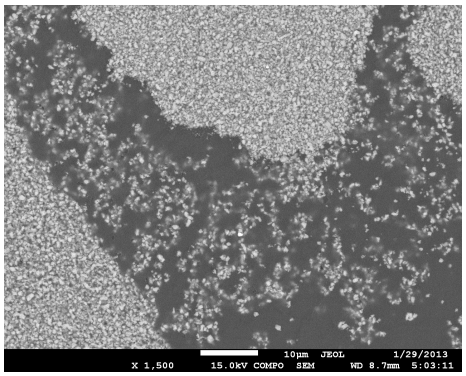

Figure 6.18: SEM micrograph of a 0-3 50vol% NTC-epoxy composite at 1500x magnification, showcasing the agglomoration of particles.

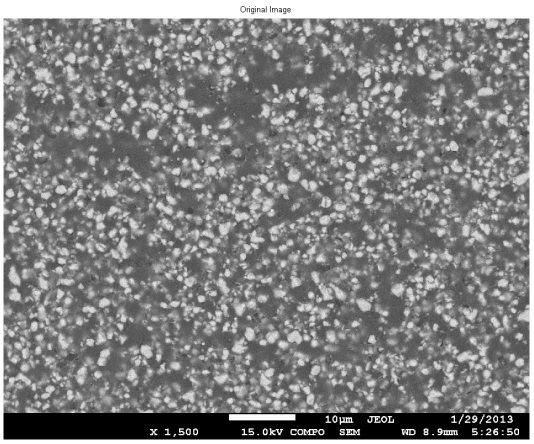

(a) Original image

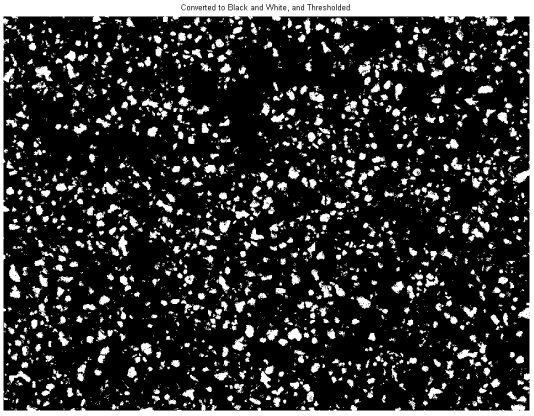

(b) Converted to black and white and thresholded

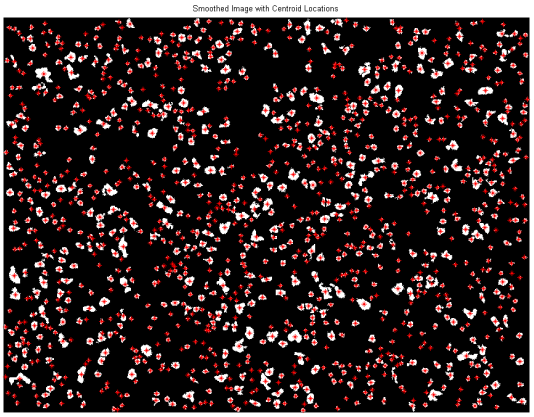

(c) Particle centroids identified of smoothed image

Figure 6.19: Image processing operations within MATLAB to identify the particles and their respective centroids within NTC polymer composites. All SEM micrographs used were at 1500x magnification.

To find out to what degree the interparticle distance of the NTC polymer composites changes as a function of the filler volume content, a SEM micrograph of each type of composite is taken at 1500x magnification and processed with MATLAB. First the original image is cropped and thresholded until only the particles in the foreground of the image remain (shown in Figure 6.19). Particles on the edge of the image are removed, holes inside each particle are filled, particles smaller than 1μm are removed, and the boundary of each remaining particle is smoothed. Next, each particle is labeled, and the centroid of each particle, the particle size, total particle count and total covered area fraction are calculated.

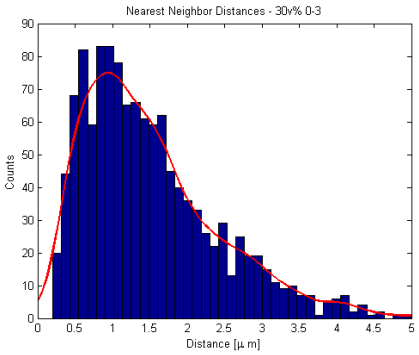

Figure 6.20: The distribution of nearest neighbor distances for a 0-3 30vol% NTC polymer composite, imaged with SEM at 1500x, and processed with MATLAB.

Then, the pair-wise distance from each centroid to each other centroid is calculated. The nearest neighbor distance of each centroid is distilled from that list, and a histogram of all the nearest neighbor distances is printed, with a kernel smoothing fit (Figure 6.20). The median nearest neighbor distance at each volume fraction of NTC, for 0-3, 1-3 and stressed composites is given in Figure 6.21 and 6.22.

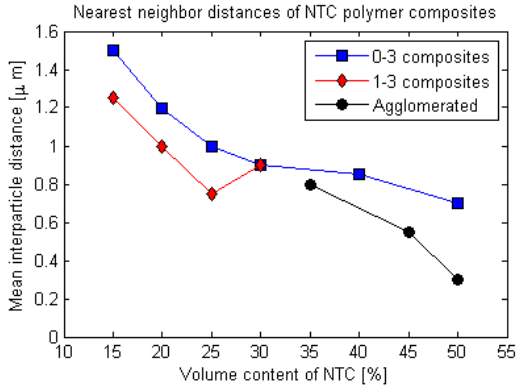

Figure 6.21: Mean interparticle distance of 0-3 and 1-3 NTC polymer composites.

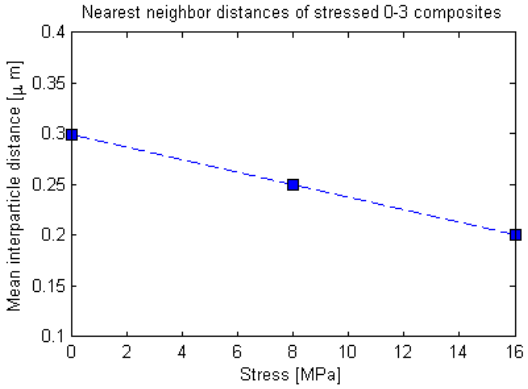

Figure 6.22: Mean interparticle distance of 0-3 50vol% stressed composites.

The interparticle distance decreases as a function of volume content and applied pressure. Structurization of the NTC particles decreases the interparticle distance at low volume fractions of NTC, but this effect tapers off as more NTC particles are added. At 30vol%, the interparticle distance of the 0-3 and 1-3 composites is the same. The agglomerated composites reach lower interparticle distances than their homogeneously mixed counterparts. At the critical volume content for percolation, 35vol%, the interparticle distance is approximately 0.8μm.

CHAPTER 7

DISCUSSION

7.1 Electrical properties of the NTC polymer composites

The obtained intrinsic resistivity and B-value results of the agglomerated negative temperature coefficient of resistance (NTC) polymer composites show that it is possible to produce electrically conductive NTC polymer composites made from nickel manganite and epoxy. The best nickel manganite/epoxy composites presented in this study have resistivities of $10^5\Omega$.cm, and B-values of $\approx$1500K, while sintered ceramics made from the same powder can easily attain $10^3\Omega$.cm and 3500K. The increased resistivity of the NTC polymer composites could be explained by the small particle size of the composites, constricting the flow of electricity. [65]

Another explanation presents itself in the work of Majid *et al.* [66], who presented an NTC polymer composite made from Mn_3O_4 and polyaniline (PANI), a polymer which has an intrinsic resistance of only 10^6 Ω. Their Mn_3O_4/PANI composite managed to reach resistivity values of $\approx 10^4\Omega$.cm and B-values in the range of 3610-4150 K. The ceramic component used, Mn_3O_4, is less conductive than the nickel manganites studied in this thesis, yet the resistivity of the Mn_3O_4/PANI composite is lower. Additionally, the wetting between PANI and Mn_3O_4 is poor and at high volume fractions of conductive filler this leads the composite to experience a degradation of NTC behavior. Due to these features, the Mn_3O_4/PANI is able to attain viable NTC electrical properties. Choosing an appropriate polymer component, with lower intrinsic resistivity and wetting behavior, would likely lead to a similar improvement of the electrical properties of a nickel manganite composite.

Determining the sort of polymer properties that lead to a better NTC polymer composite could be extremely beneficial. The Epotek epoxy used in this study insulates the nickel manganite particles too well when they are homogeneously mixed. If the wetting between the NTC particles and the polymer matrix could be reduced, it follows that the connectivity between the NTC particles would increase. In the agglomerated NTC composites, the increase of conductivity is due to a reduction of connectivity between the NTC particles and the polymer matrix. The interaction of the NTC particles with the polymer is decreased, as pockets of NTC powder are able to remain almost entirely divorced from the polymer's insulating effects (Figure 6.17).

A second issue with the Epotek epoxy is its high resistivity. The results from Majid *et al.* have been garnered with a polymer that has a much lower intrinsic barrier to conductivity, at 10^6 Ω. Clearly there is room for improvement of the electrical properties of NTC composites.

Measuring the NTC polymer composites at 85°C to calculate the B-value presents two further issues for characterization of the composite: the composite becomes flexible since its T_g is at 55°C, and the electrode adhesion worsens.

Proper electrode adhesion of electrically conductive composites is notoriously difficult to maintain. [64, 67–69] In some cases, the gold electrode layer on the NTC composites was already unstable immediately after sputtering. Even though new gold was sputtered on each NTC composite sample before every measurement, it is possible that the B-value measurements may be inaccurate, considering that gold may have dissolved into the oil, and incomplete electrodes were used during the measurement. Secondly, since the measurement at 85°C is above the T_g of the epoxy, the mechanical flexibility of each composite increases during the measurement, which stretches and damages the electrode layer.

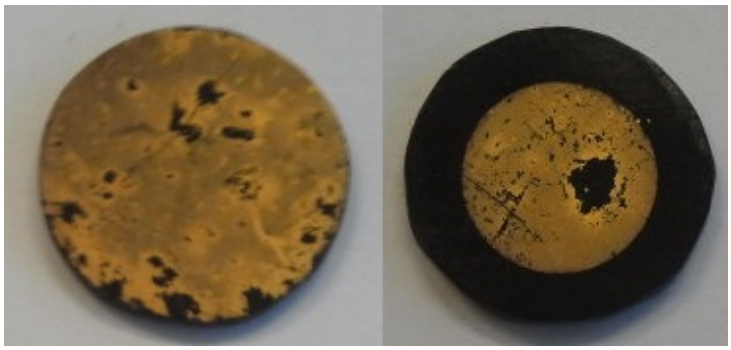

Figure 7.1: Electrode adhesion on NTC composites after measuring resistance at 85°C in oil.

The nearest neighbor interparticle distance calculated in section 6.5 is an indicator of the degree of connectivity between the NTC particles. [65] In the 0-3 composites, both the interparticle distance and the resistivity decrease with increasing volume of NTC particles, similar to the behavior of 0-3 lead zirconium titanate (PZT) composites until it plateaus at approximately 0.75μm. Only the interparticle distance of the agglomerated composites reaches the low distance of 0.3μm that the PZT composites would lead one to expect. [70] Furthermore, in the agglomerated composites, the arrangement of the NTC particles between agglomerates appears to be similar to the tree-like structures common in carbon black composites, known to decrease the percolation limit (Figure 6.17). [65]

In the stressed NTC composites, hot-pressing the NTC polymer composites after they have already cured increases the conductivity, corresponding to the results of Yoshikawa *et al.* [64]. The internal stresses of the polymer matrix caused by shrinkage are known to play a role in the conductivity of composites. [59, 64, 65] However, these results would seem to indicate that producing NTC polymer composites by hot-pressing could increase the electrical conductivity. Similar to the effect of DEP, forcing the particles closer together without having to strain the polymer matrix would decrease the interparticle distance, increasing conductivity. The influence of the mechanical and thermal properties of the polymer matrix on the electrical behavior of NTC polymer composites requires further study.

Finally, by definition the image processing method used to find the interparticle distance from the scanning electron microscope (SEM) micrographs in MATLAB is not entirely accurate. Thresholding and smoothing the images leads to loss of pixel information. Removing particles on the edge of the images, while necessary, also reduces the amount of nearest neighbor particles, potentially synthetically increasing the median nearest neighbor distance.

7.2 Structured composites

Even though the conductivity of the nickel manganite composites is not significantly affected by dielectrophoresis (DEP), it is clear that chains of particles can be induced to form from the SEM investigation (Figure 6.8) and DEP demonstration (6.16). Dielectrophoresis is already employed to align carbon nano tubes [71], so it comes as no surprise that the semiconducting NTC particles can be aligned.

The interparticle distance of the 1-3 composites is lower than in the 0-3 composites of equal filler volume, but the reduction is not as marked as it is for structured PZT composites. The interparticle distance of the 1-3 PZT composites was reported to be a near constant distance of 0.3μm at every volume fraction, while the interparticle distance of the 1-3 NTC composites remains within the much higher range of $0.9 - 1.2\mu$m. At an interparticle distance of 0.3μm the NTC composite conducts. That is the interparticle distance of the agglomerated 50vol% NTC composites. It stands to reason that if the effect of DEP can be amplified, the $\approx 10^5\Omega$.cm attained at high volume fractions in these NTC polymer composites could also be attained at lower volume fractions. The short circuit shown in Figure 6.9 illustrates this point, since it shows that DEP can create fully conducting continuous chains of NTC particles, if the interparticle distance can be decreased enough.

7.3 Modeling connectivity

The homogeneously mixed 0-3 composites do not switch from series connectivity to parallel connectivity, as the Lichtenecker plot of the resistivity of all NTC composites shows (Figure 7.2). The agglomerated NTC composites do switch to near-parallel connectivity with an n value of approximately 0.35.

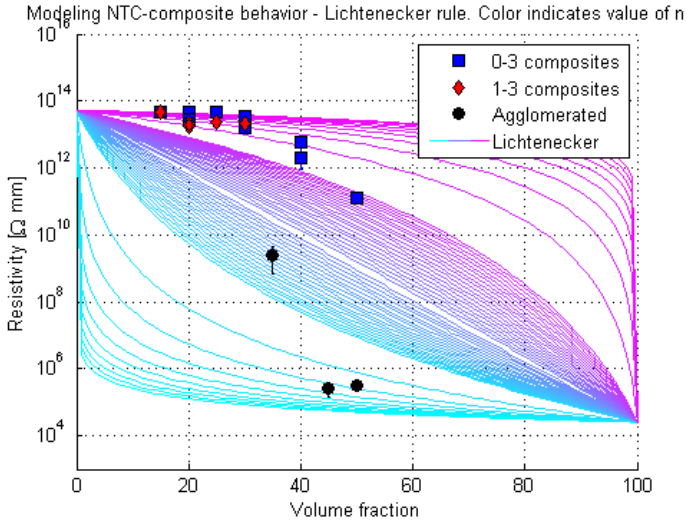

Figure 7.2: Resistivity at 25C of 0-3, 1-3 and agglomerated NiMnO and Epotek epoxy composites compared to the Lichtenecker addition model. The color of the Lichtenecker plot indicates the value of n.

The percolation limit of the homogeneous 0-3 composite lies above the highest volume fraction composites prepared during this study (at 50vol%), since even at 50vol%, the NTC polymer composites still appear to experience series conductivity (Figure 7.2). To decrease the percolation limit, the particle size could be reduced. [63] However, this will increase the constriction resistance (since it is

a function of particle contact spot diameter), decreasing the resistivity of the NTC polymer composite. [65]

The percolation behavior of the NTC composites can also be influenced by the shape of the filler. In general, replacing spherical particles by high aspect ratio particles, or fibers, results in a drastic decrease in the percolation limit. [65]

The NTC particle size examined in this study was in the range of 1 - 10μm, chosen for best DEP performance. To ascertain whether a change in the particle size and shape will positively affect the percolation of homogeneous 0-3 NTC polymer composites without reducing their electrical properties, new NTC particles will have to be milled to sub-micron sizes.

The wetting of the polymer and the NTC is remarkably high and inhibits percolation. The NTC-epoxy stacks show that the epoxy layer between conducting NTC ceramics has a considerable effect on the ultimate electrical properties of the composite. The nearest neighbor interparticle distance of the NTC composites must remain below a certain distance, but the increased conductivity of the agglomerated composites would seem to indicate that there is also an added benefit of creating a network structure of NTC particles of varying sizes. In this case, agglomerates of $\approx 100\mu$m and loose particles bridging gaps between agglomerates of $\approx 10\mu$m.

7.4 Conclusions

Although the Epotek epoxy used in this study has a low dielectric constant, an attractive quality for DEP, the high resistivity and wetting with the NTC particles appear to form a barrier which is too high for homogeneously mixed NTC polymer composites to overcome. Only the agglomerated NTC polymer composites have shown to have the appropriate electrical properties, emulating parallel conductivity. The NTC particles inside the agglomerates experience much less interaction with the polymer, so it follows that the conductivity within the agglomerated NTC polymer composites is capable of becoming much higher.

The NTC polymer composites presented here could possibly be improved by examining the effect of reducing the NTC particle size to decrease the percolation limit, testing polymers with lower intrinsic resistivity and wetting properties, and alternate production processes.

CHAPTER 8

GENERAL CONCLUSIONS

In this thesis the prospects of developing a negative temperature coefficient of resistance (NTC) polymer composite thermistor have been investigated as well as the stability and phase formation of traditional NTC ceramics.

The investigations into NTC ceramics confirm that the cooling conditions have a strong influence on both the electrical properties of NTC ceramics and the stability. NTC ceramics produced by quenching and stoichiometrically cooling, and those with a nickel oxide second phase, are the most stable, as indicated by the 125°C aging study.

The concept of functional granular composites (FGC)'s has been known for some time, but has seldom been applied to conducting fillers that already have an NTC of their own. A method to produce an NTC thermistor composite has been developed by combining a calcined nickel manganite NTC powder with an epoxy matrix. The lowest resistivity in these NTC polymer composites is in the range of $10^5\Omega$.cm, attained for agglomerated high filler volume fraction composites.

It turns out that the characteristics of both the filler and the polymer matrix influence the electrical properties of the composite. The particle size and morphology of the NTC filler have a strong influence on the percolation limit and the resistivity of the composite. At the particle size used for these NTC composites, 1 to 10μm, the percolation limit is relatively high (35vol%). The resistivity of the NTC composite appears to be constricted by the small particle size, since the resistance of composite is still orders of magnitude above that of the bulk ceramic.

The interparticle distance, which is also a function of particle size, further influences the percolation limit and electrical behavior. A decreased interparticle distance results in a smaller volume of entrapped polymer matrix material and an increase in conductivity. The interparticle distance in nickel manganite epoxy composites is decreased by increasing the filler volume content, applying structurization and allowing the filler to agglomerate.

Quantifying the influence of the mechanical, electrical and thermal properties of the polymer matrix chosen for an NTC polymer composite and the effect on the ultimate electrical behavior requires further research. It is clear that the wetting and intrinsic resistivity of the polymer matrix strongly influences the conductivity of the NTC polymer composite. Internal stresses in the polymer matrix, induced via hot pressing, also strongly influence the conductivity of NTC polymer composites.

A logical next step in understanding the influence of the filler on NTC polymer composites would be to vary the size and shape of the NTC particles. Cycling the temperature to find the actual curve of the B-value as well as the stability of the NTC behavior would also provide vital information. Furthermore, it is recommended to investigate the influence of polymers with high shrinkage, low intrinsic resistivity and poor wetting on the electrical properties of NTC polymer composites.

NTC particles can be induced by dielectrophoresis (DEP) to align themselves into chains in an epoxy matrix. In future work, once the influence of the NTC filler and polymer matrix is better understood, DEP could become a viable option to produce flexible NTC polymer composites.

ACKNOWLEDGMENTS

This master's thesis represents the culmination of my time as a student at Aerospace Engineering at the TU Delft. I am happy to present our results, and I hope you had as much pleasure reading them as we did in producing them.

I would like to take this opportunity to thank all the people who helped to make this thesis possible, starting with my supervisors Pim Groen and Sybrand van der Zwaag who always made time for me and motivated me to improve and refine my research. Furthermore, I would like to thank both Hamideh Khanbareh and Nijesh K. James who acted as my (unofficial) daily supervisors throughout my thesis work, without whom this thesis may never have been finished. Special thanks also goes to the tireless technicians from the workshop and aircraft hall, who always took the time to help me, no matter my request.

In my experience, much like raising children, it takes a village to raise an engineer, and my 'village' is populated with wonderful people. Thank you to: Jelmer, Ariane, Casper, Jasper, Kinge, everyone present at the infamous NovAM coffee breaks, and of course my parents for always supporting me and listening to my research related rantings.

BIBLIOGRAPHY

[1] A. Feteira, "Negative Temperature Coefficient Resistance (NTCR) ceramic thermistors: An industrial perspective," *Journal of the American Ceramic Society*, vol. 92, no. 5, pp. 967–983, 2009.

[2] C. J. Yeager and S. S. Courts, "A review of cryogenic thermometry and common temperature sensors," *IEEE Sensors Journal*, vol. 1, no. 4, pp. 352–360, 2001.

[3] P. R. N. Childs, J. R. Greenwood, and C. A. Long, "Review of temperature measurement," *Review of Scientific Instruments*, vol. 71, no. 8, p. 2959, 2000.

[4] E. D. Macklen, "Chapter 1: NTC materials and their fundamental properties," in *Thermistors*, pp. 4–15, Ayr, Scotland: Electromechanical publications Ltd., 1975.

[5] D. G. Wickham, "Solid-phase equilibria in the system NiO-Mn2O3-O2," *Journal of Inorganic Nuclear Chemistry*, vol. 26, no. 1958, 1964.

[6] A. Elham, "Structural Design: Weight Estimation," in *Encyclopedia of Aerospace Engineering*, 2012.

[7] J. Fraden, "Chapter 16: Temperature sensors," in *Handbook of Modern Sensors*, pp. 519–565, SpringerLink, 2010.

[8] W. H. Bragg, "The structure of the spinel group of crystals," *Philosophical Magazine*, vol. 30, no. 175-180, pp. 305–315, 1915.

[9] S. Nishikawa, "Structure of some crystal of the spinel group," *Proc. Math. Phys. Soc. Tokyo*, vol. 8, pp. 199–209, 1915.

[10] C. Kittel, *Introduction to solid state physics*. John Wiley & Sons, Inc., 1957.

[11] A. Petric and H. Ling, "Electrical conductivity and thermal expansion of spinels at elevated temperatures," *Journal of the American Ceramic Society*, vol. 90, no. 5, pp. 1515–1520, 2007.

[12] E. J. W. Verwey and E. L. Heilmann, "Physical properties and cation arrangement of oxides with spinel structures: I. Cation arrangement in spinels," *The Journal of Chemical Physics*, vol. 15, no. 4, p. 174, 1947.

[13] H. W. Jaffe, *Crystal chemistry and refractivity*. London, United Kingdom: Constable and Company, Ltd., 1996.

[14] H. A. Jahn and E. Teller, "Stability of polyatomic molecules in degenerate electronic states: I. Orbital degeneracy," *Proceedings of the Royal Society A: Mathematical, Physical and Engineering Sciences*, vol. 161, no. 905, pp. 220–235, 1937.

[15] J. Dunitz and L. Orgel, "Electronic properties of transition-metal oxides: II. Cation distribution amongst octahedral and tetrahedral sites," *Journal of Physics and Chemistry of Solids*, vol. 3, pp. 318–323, 1957.

[16] E. G. Larson, R. J. Arnott, and D. G. Wickham, "Preparation, semiconduction and low-temperature magnetization of the system Ni1-xMn2+xO4," *Journal of Physics and Chemistry Solids*, vol. 23, pp. 1771–1781, 1962.

[17] F. de Boer, J. H. van Santen, and E. J. W. Verwey, "The Electrostatic Contribution to the Lattice Energy of Some Ordered Spinels," *The Journal of Chemical Physics*, vol. 18, no. 8, p. 1032, 1950.

[18] EPCOS, "NTC Thermistors: General technical information," Tech. Rep. February, EPCOS A9, 2009.

[19] E. J. W. Verwey, P. W. Haayman, and F. C. Romeijn, "Physical properties and cation arrangement of oxides with spinel structures: II. Electronic conductivity," *The Journal of Chemical Physics*, vol. 15, no. 4, p. 181, 1947.

[20] H. L. Tuller and A. S. Nowick, "Small polaron electron transport in reduced CeO2 single crystals," *Journal of Physics and Chemistry of Solids*, vol. 38, pp. 859–867, 1977.

[21] S. E. Dorris and T. O. Mason, "Electrical properties and cation valencies in Mn304," *Journal of the American Ceramic Society*, vol. 71, no. 5, pp. 379–385, 1988.

[22] R. Metz, "Electrical properties of NTC thermistors made of manganite ceramics of general spinel structure: Mn 3-x-x'MxNxO4 (0-x+x'-1; M and N being Ni, Co or Cu). Aging phenomenon study," *Journal of Materials Science*, vol. 35, pp. 4705–4711, 2008.

[23] H. K. Bowen and T. O. Mason, "Electronic conduction and thermopower of magnetite and iron-aluminate spinels," *Journal of the American Ceramic Society*, vol. 64, pp. 237–242, 1980.

[24] W. A. Groen, C. Metzmacher, P. Huppertz, and S. Schuurman, "Aging of NTC ceramics in the system Mn-Ni-Fe-O," *Journal of Electroceramics*, vol. 7, pp. 77–87, 2001.

[25] R. Heikes, *Thermoelectricity: Science and engineering*. New York, NY: Interscience Publishers, 1961.

[26] S. T. Kshirsagar, "Electrical and crystallographic studies of the system CuxNi1-xMn2O4," *Journal of the Physical Society of Japan*, vol. 27, no. 5, pp. 1164–1170, 1969.

[27] M. Suzuki, "A.c. hopping conduction in Mn-Co-Ni-Cu complex oxide semiconductors with spinel structure," *Journal of Physics and Chemistry of Solids*, vol. 41, pp. 1253–1260, 1980.

[28] R. Metselaar, R. E. J. van Tol, and P. Piercy, "The Electrical Conductivity and Thermoelectric Power of Mn304 at High Temperatures," *Journal of Solid State Chemistry*, vol. 38, pp. 335–341, 1981.

[29] V. A. M. Brabers and J. C. J. M. Terhell, "Electrical conductivity and cation valencies in nickel manganite," *Physica Status Solidi (a)*, vol. 69, no. 325, pp. 325–332, 1982.

[30] B. Gillot, M. Kharroubi, R. Metz, R. Legros, and A. Rousset, "Electrical properties and cationic distribution in cubic nickel manganite spinels NixMn3-xO4, 0.57-x-1," *Solid State Ionics*, vol. 44, pp. 275–280, 1991.

[31] T. Sasamoto, T. Meguro, T. Yokoyama, Y. Abe, and M. Torikai, "Crystal structure and electrical property of Mn-Fe-Co-Ni oxide for thermistor materials in the manufacture process," *Key Engineering Materials*, vol. 53-55, pp. 101–106, 1991.

[32] J. Töpfer, A. Feltz, P. Dordor, and J. P. Doumerc, "Thermopower analysis of substituted nickel manganite spinels," *Materials Research Bulletin*, vol. 29, no. 3, pp. 225–232, 1994.

[33] A. Amin and R. Newnham, "Thermistors," *Key Engineering Materials*, vol. 66-67, pp. 339–373, 1992.

[34] H. Altenburg, O. Mrooz, J. Plewa, O. Shpotyuk, and M. Vakiv, "Semiconductor ceramics for NTC thermistors: The reliability aspects," *Journal of the European Ceramic Society*, vol. 21, no. 10-11, pp. 1787–1791, 2001.

[35] S. Fritsch, J. Sarrias, M. Brieu, J. J. Couderc, J. L. Baudour, E. Snoeck, and A. Rousset, "Correlation between the structure, the microstructure and the electrical properties of nickel manganite negative temperature coefficient (NTC) thermistors," *Solid State Ionics*, vol. 109, pp. 229–237, 1998.

[36] P. Castelan, B. Ai, A. Loubiere, A. Rousset, and R. Legros, "Aging study of nickel-copper-manganite negative temperature coefficient thermistors by thermopower measurements," *Journal of Applied Physics*, vol. 72, pp. 4705–4709, 1992.

[37] T. Battault, R. Legros, M. Brieu, J. J. Couderc, L. Bernard, and A. Rousset, "Correlation between microstructure and ageing of iron manganite thermistors," *Journal de Physique III*, vol. 7, pp. 979–992, 1997.

[38] Z. Wang, C. Zhao, P. Yang, L. Winnubst, and C. Chen, "Effect of annealing in O2 or N2 on the aging of Fe0.5Mn1.84Ni0.66O4 NTC-ceramics," *Solid State Ionics*, vol. 177, no. 19-25, pp. 2191–2194, 2006.

[39] D.-l. Fang, C.-h. Zheng, C.-s. Chen, and A. J. A. Winnubst, "Aging of nickel manganite NTC ceramics," *Journal of Electroceramics*, vol. 22, no. 4, pp. 421–427, 2008.

[40] C. Metzmacher, W. A. Groen, and I. M. Reaney, "Microstructure and electrical properties of Mn-Ni-In spinels," *Physica Status Solidi (a)*, vol. 181, pp. 369–386, 2000.

[41] T. Battault, R. Legros, and A. Rousset, "Aging of iron manganite negative temperature coefficient thermistors," *Journal of Materials Research*, vol. 13, no. 5, pp. 1238–1242, 1998.

[42] W. A. Groen, V. Zaspalis, and S. Schuurman, "Aging of NTC ceramics investigated by magnetic measurements," *Journal of Materials Science Letters*, vol. 18, pp. 1233–1235, 1999.

[43] G. Csete de Györgyfalva, A. Nolte, and I. Reaney, "Correlation between microstructure and conductance in NTC thermistors produced from oxide powders," *Journal of the European Ceramic Society*, vol. 19, no. 6-7, pp. 857–860, 1999.

[44] S. Fritsch, C. Chanel, J. Sarrias, S. Bayonne, A. Rousset, X. Alcobe, and M. L. M. Sarrion, "Structure, thermal stability and electrical properties of zinc manganites," *Solid State Ionics*, vol. 128, pp. 233–242, 2000.

[45] A. Feltz and W. Po, "Spinel forming ceramics of the system FexNiyMn3-x-yO4 for high temperature NTC thermistor applications," *Journal of the European Ceramic Society*, vol. 20, pp. 2353–2366, 2000.

[46] O. Mrooz, I. Hadzaman, M. Vakiv, O. Shpotyuk, J. Plewa, H. Altenburg, and H. Uphoff, "Aging of copper-nickel-cobalt manganite NTC thermistors," in *23rd International Conference on Microelectrics (MIEL 2002)*, vol. 1, pp. 12–15, 2002.

[47] M. Vakiv, O. Shpotyuk, V. Balitska, B. Butkiewicz, and L. Shpotyuk, "Ageing behavior of electrical resistance in manganite NTC ceramics," *Journal of the European Ceramic Society*, vol. 24, no. 6, pp. 1243–1246, 2004.

[48] V. O. Balitska, B. Butkievich, O. Shpotyuk, and M. Vakiv, "On the analytical description of ageing kinetics in ceramic manganite-based NTC thermistors," *Journal of Non-Crystalline Solids*, vol. 42, no. 2002, pp. 2003–2007, 2007.

[49] S. Liang, J. Yang, X. Yi, X. Zhang, and Y. Bai, "An efficient way to improve the electrical stability of Ni0.6Si0.2Al0.6Mn1.6O4 NTC thermistor," *Ceramics International*, vol. 37, no. 7, pp. 2537–2541, 2011.

[50] A. Navrotsky and O. J. Kleppa, "The thermodynamics of cation distributions in simple spinels," *Journal of Inorganic Nuclear Chemistry*, vol. 29, pp. 2701–2714, 1967.

[51] E. Elbadraoui, J. Baudour, C. Leroux, S. Fritsch, F. Bouree, B. Gillot, and A. Rousset, "Cation distribution, short-range order and small polaron hopping conduction in nickel manganites, from a neutron diffraction study," *Physica Status Solidi (B)*, vol. 212, no. 1, pp. 129–139, 1999.

[52] S. Fritsch, *Role des traitements thermiques sur les proprietes structurales, microstructurales et electriques de manganites de metaux de transition. Application au vieillissement des themistances a coefficient de temperature negatif (NTC).* PhD thesis, 1995.

[53] S. Fritsch, J. Salmi, J. Sarrias, A. Rousset, S. Schuurman, and A. Lannoo, "Mechanical properties of nickel manganites-based ceramics used as negative temperature coefficient thermistors (NTC)," *Materials Research Bulletin*, vol. 39, no. 12, pp. 1957–1965, 2004.

[54] C. Julien, M. Massot, and C. Poinsignon, "Lattice vibrations of manganese oxides - Part I. Periodic structures," *Spectrochimica Acta Part A: Molecular and Biomolecular Spectroscopy*, vol. 60, no. 3, pp. 689–700, 2004.

[55] R. E. Newnham, D. P. Skinner, and L. E. Cross, "Connectivity and piezoelectric-pyroelectric composites," *Materials Research Bulletin*, vol. 13, pp. 525–536, 1978.

[56] A. Safari, "Development of piezoelectric composites for transducers," *Journal de Physique III*, vol. 4, pp. 1129–1149, 1994.

[57] D. A. van den Ende, B. F. Bory, W. A. Groen, and S. van der Zwaag, "Improving the d33 and g33 properties of 0-3 piezoelectric composites by dielectrophoresis," *Journal of Applied Physics*, vol. 107, no. 2, p. 024107, 2010.

[58] S. E. van Kempen, "Literature study: Modeling of microstructural imperfections in piezoelectric composite materials," tech. rep., TU Delft, 2012.

[59] R. E. Newnham, "Composite electroceramics," *Ferroelectrics*, vol. 68, no. 1, pp. 1–32, 1986.

[60] D. S. Mclachlan, M. Blaszkiewicz, and R. E. Newnham, "Electrical Resistivity of Composites," *Journal of the American Ceramic Society*, vol. 73, no. 8, pp. 2187–2203, 1990.

[61] G. R. Ruschau, S. Yoshikawa, and R. E. Newnham, "Resistivities of conductive composites," *Journal of Applied Physics*, vol. 72, no. 3, pp. 953–959, 1992.

[62] H. Wagar, *Physical Design of Electronic Systems*. Prentice Hall, Englewood Cliffs, NJ, vol. 3 ed., 1971.

[63] G. Ruschau, S. Yoshikawa, and R. Newnham, "Percolation constraints in the use of conductor-filled polymers for interconnects," *Proceedings 42nd Electronic Components & Technology Conference*, pp. 481–486, 1992.

[64] S. Yoshikawa, T. Ota, R. Newnham, and A. Amin, "Piezoresistivity in polymer-ceramic composites," *Journal of the American Ceramic Society*, vol. 73, no. 2, pp. 263–267, 1990.

[65] R. Strumpler and J. Glatz-Reichenbach, "Conducting Polymer Composites," *Journal of Electroceramics*, vol. 3, no. 4, pp. 329–346, 1999.

[66] K. Majid, S. Awasthi, and M. Singla, "Low temperature sensing capability of polyaniline and Mn3O4 composite as NTC material," *Sensors and Actuators A: Physical*, vol. 135, no. 1, pp. 113–118, 2007.

[67] J. Song, J.-H. Jeon, I.-K. Oh, and K. C. Park, "Electro-active Polymer Actuator Based on Sulfonated Polyimide with Highly Conductive Silver Electrodes Via Self-metallization.," *Macromolecular rapid communications*, pp. 1583–1587, 2011.

[68] R. Strumpler, "Polymer composite thermistors for temperature and current sensors," *Journal of Applied Physics*, vol. 80, no. 11, p. 6091, 1996.

[69] J. Chilton and G. Garner, "Ferroelectrics Adhesion in electroactive composites," no. January 2013, pp. 37–41, 2011.

[70] D. A. van den Ende, *Structured piezoelectric composites: Materials and applications*. PhD thesis, 2012.

[71] W. Xue and P. Li, "Dielectrophoretic Deposition and Alignment of Carbon Nanotubes," in *Carbon Nanotubes - Synthesis, Characterization, Applications* (S. Yellampalli, ed.), pp. 171–190, 2009.

APPENDIX A

REPORTED CATION DISTRIBUTIONS OF NICKEL MANGANITES

Year	Investigators	Techniques	Cation distribution
1957	Bongers	Magnetic measurements	$Mn^{2+}[Ni^{2+}Mn^{4+}]O_4^{2-}$
1957	Sinha et al.	X-ray diffraction (XRD)	$Mn^{2+}[Ni^{2+}Mn^{4+}]O_4^{2-}$
1958	Baltzer and White	XRD and magnetic measurements	$Mn^{2+}[Ni^{2+}Mn^{4+}]O_4^{2-}$
1959	Azaroff	Neturon diffraction	$Mn^{3+}[Ni^{2+}Mn^{3+}]O_4^{2-}$
1961	O'Keefe	Crystal field theory	$Mn_x^{2+}Mn_{1-x}^{3+}[Ni_{1-x}^{2+}Mn_{1-x}^{3+}]O_4^{2-}$
1962	Larson et al.	XRD, electrical conductivity, Seebeck and magnetic measurements	$Mn_{0.65}^{2+}Mn_{0.35}^{3+}[Ni^{2+}Mn_{0.35}^{3+}]O_4^{2-}$
1969	Boucher et al.	Magnetic and neutron measurements	$Ni_{1-y}^{2+}Mn_y^{3+}[Ni_v^{2+}Mn_{2-v}^{3+}]O_4^{2-}$
1972	Brabers	Infrared	$Mn_y^{2+}Ni_{1-y}^{2+}[Ni_y^{2+}Mn_{2-2y}^{3+}Mn_y^{4+}]O_4^{2-}$
1976	Bhandage and Keer	XRD, ESR, electrical conductivity, and Seebeck measurements	$Mn^{3+}[Ni^{2+}Mn_{0.1}^{2+}Mn_{0.9}^{3+}]O_{3.95}^{2-}$
1982	Brabers and Terhell	Electrical conductivity, thermopower, and thermal expansion measurements	$Ni_{1-v}^{2+}Mn_v^{2+}[Ni_v^{2+}Mn_{2-2v}^{3+}Mn_v^{4+}]O_4^{2-}$
1983	Brabers et al.	X-ray photoelectron spectroscopy	$Ni_{1-v}^{2+}Mn_v^{2+}[Ni_v^{2+}Mn_{2-2v}^{3+}Mn_v^{4+}]O_4^{2-}$
1986	Macklen	Electrical measurements and thermobalance	$Ni_{0.35}^{2+}Mn_{0.65}^{2+}[Ni_{0.65}^{2+}Mn_{0.70}^{3+}Mn_{0.65}^{4+}]O_4^{2-}$
1987	Golestani et al.	XRD	$Ni_{0.17}^{2+}Mn_{0.83}^{2+}[Ni_{0.49}^{2+}Mn_{1.66}^{3+}]O_4^{2-}$
1988	Islam and Catlow	Computational methods	$Ni_{1-v}^{2+}Mn_v^{3+}[Ni_v^{2+}Mn_{2-2v}^{3+}]O_4^{2-}$
1997	Laberty et al.	Wide angle X-ray scattering	$Ni_{0.21}^{2+}Mn_{0.29}^{2+}\nabla_{0.5}[Ni_{0.37}^{2+}Ni_{0.25}^{3+}Mn_{1.37}^{4+}]O_4^{2-}$

Table A.1: Cation distributions proposed for $NiMn_2O_4$. [1]